9-21-2015

# Ionospheric Response to Infrasonic-Acoustic Waves Generated by Natural Hazard Events

M. D. Zettergren
*Embry-Riddle Aeronautical University*, zettergm@erau.edu

J. B. Snively
*Embry-Riddle Aeronautical University*, snivelyj@erau.edu



## Scholarly Commons Citation

Zettergren, M. D., & Snively, J. B. (2015). Ionospheric Response to Infrasonic-Acoustic Waves Generated by Natural Hazard Events. *Journal of Geophysical Research: Space Physics, 120*(9). https://doi.org/10.1002/2015JA021116

AGU PUBLICATIONS

JGR

Journal of Geophysical Research: Space Physics

RESEARCH ARTICLE

10.1002/2015JA021116

**Key Points:**
- Ionospheric responses to infrasound depend on local magnetic field geometry
- Directivity of natural hazard wave sources impacts ionospheric responses
- TEC responses are strongest equatorward of source, current responses poleward

**Correspondence to:**
M. Zettergren,
zettergm@erau.edu

**Citation:**
Zettergren, M. D., and J. B. Snively (2015), Ionospheric response to infrasonic-acoustic waves generated by natural hazard events, *J. Geophys. Res. Space Physics*, *120*, 8002–8024, doi:10.1002/2015JA021116.

Received 11 FEB 2015
Accepted 5 AUG 2015
Accepted article online 12 AUG 2015
Published online 21 SEP 2015



# Ionospheric response to infrasonic-acoustic waves generated by natural hazard events

**M. D. Zettergren[1] and J. B. Snively[1]**

[1]Department of Physical Sciences, Embry-Riddle Aeronautical University, Daytona Beach, Florida, USA

**Abstract** Recent measurements of GPS-derived total electron content (TEC) reveal acoustic wave periods of ~1–4 min in the *F* region ionosphere following natural hazard events, such as earthquakes, severe weather, and volcanoes. Here we simulate the ionospheric responses to infrasonic-acoustic waves, generated by vertical accelerations at the Earth's surface or within the lower atmosphere, using a compressible atmospheric dynamics model to perturb a multifluid ionospheric model. Response dependencies on wave source geometry and spectrum are investigated at middle, low, and equatorial latitudes. Results suggest constraints on wave amplitudes that are consistent with observations and that provide insight on the geographical variability of TEC signatures and their dependence on the geometry of wave velocity field perturbations relative to the ambient geomagnetic field. Asymmetries of responses poleward and equatorward from the wave sources indicate that electron perturbations are enhanced on the equatorward side while field aligned currents are driven principally on the poleward side, due to alignments of acoustic wave velocities parallel and perpendicular to field lines, respectively. Acoustic-wave-driven TEC perturbations are shown to have periods of ~3–4 min, which are consistent with the fraction of the spectrum that remains following strong dissipation throughout the thermosphere. Furthermore, thermospheric acoustic waves couple with ion sound waves throughout the *F* region and topside ionosphere, driving plasma disturbances with similar periods and faster phase speeds. The associated magnetic perturbations of the simulated waves are calculated to be observable and may provide new observational insight in addition to that provided by GPS TEC measurements.

## 1. Introduction

The atmospheric and ionospheric responses to "acoustic and gravity waves generated by impulsive forcing" events have been well appreciated for decades [e.g., *Yeh and Liu*, 1974, and references therein]. Acoustic waves with periods of minutes are generated by processes that occur over time scales short enough to compress, rather than displace, the atmosphere. Recent studies, leveraging measurements of ionospheric total electron content (TEC) from ground-based GPS networks, readily detect acoustic waves in the *F* region ionosphere generated by convective updrafts [e.g., *Nishioka et al.*, 2013] and impulsive forcing associated with natural hazard events including volcanic eruptions [e.g., *Dautermann et al.*, 2009a] and earthquakes [e.g., *Matsumura et al.*, 2011].

Early radio measurements of the ionosphere reported periodicities of ~1–5 min above convective weather systems, which were attributed to acoustic and acoustic-gravity waves [e.g., *Baker and Davies*, 1969; *Georges*, 1973]. Waves above the Brunt-Väisälä frequency (>3.3 mHz, periods <5 min) have also been detected in mesospheric airglow spectral data [*Pilger et al.*, 2013a, 2013b], consistent with acoustic or evanescent waves near the acoustic cutoff frequency; remote sensing of the *D* region likewise reveals short acoustic and gravity wave periods [*Lay and Shao*, 2011; *Marshall and Snively*, 2014]. Recent GPS observations of ionospheric TEC following the Moore, Oklahoma EF5 tornado-producing storm revealed ~4 min periodicities southward of the storm center [*Nishioka et al.*, 2013], illustrating clearly the direct spatial and temporal connections between tropospheric weather and localized periodic disturbances of the *F* region ionosphere.

Detections of waves generated by natural hazard events, and volcanoes in particular, were brought to scientific attention following the 1980 eruption of Mount St. Helens. Acoustic and gravity wave perturbations were observable across the globe via microbarographs and radio methods [*Roberts et al.*, 1982]; compressional Lamb waves with periods ~5 min and gravity waves with periods ~10s of minutes were observed thousands of kilometers from the source [*Liu et al.*, 1982]. As with observations of convective forcing, similar acoustic

periods ~3.5–5.5 min were also reported by *Delclos et al.* [1990]. More recent studies of the Soufrière Hills Volcano in Montserrat by *Dautermann et al.* [2009a, 2009b] also reveal clear GPS TEC signatures with ~4 min periods, the amplitudes of which provide estimates of energy release. These persistent signatures, and similar responses observed after earthquakes, have been attributed to atmospheric acoustic resonance [e.g., *Artru et al.*, 2001; *Saito et al.*, 2011, and references therein].

Earthquakes are a known source of ionospheric disturbances [e.g., *Calais and Bernard Minster*, 1995; *Matsumura et al.*, 2011]. As a secondary effect of earthquake forcing, it was also postulated by *Hines* [1972] that associated tsunamis may be capable of producing atmospheric gravity waves that could subsequently propagate to high altitudes. Of most recent attention was the 11 March 2011, magnitude 9.0 earthquake and resulting tsunami that caused catastrophic damage along the coastal region of Tohoku, Japan. This event induced significant measurable perturbations to the atmosphere and ionosphere, which have been reported in recent literature [*Liu et al.*, 2011; *Rolland et al.*, 2011; *Maruyama et al.*, 2011; *Occhipinti et al.*, 2011; *Makela et al.*, 2011; *Galvan et al.*, 2012]. The forcing mechanisms for the observed acoustic and gravity waves include a complex superposition of processes, including the localized sea surface perturbations due to the earthquake, producing both acoustic and gravity waves [e.g., *Saito et al.*, 2011; *Matsumura et al.*, 2011], and the outward traveling tsunami waves [e.g., *Occhipinti et al.*, 2011; *Galvan et al.*, 2012].

GPS network observations of natural hazard-related TEC perturbations reveal unprecedented detail into the spatial structure of wave fields and responses and have indicated that observed signatures are more pronounced in the magnetic equatorward direction from the source. This feature has been present in connection with a wide range of physical sources including, for example, volcanoes [*Heki*, 2006], weather events [*Nishioka et al.*, 2013], earthquakes [*Heki and Ping*, 2005; *Saito et al.*, 2011], and even rocket launches [*Ding et al.*, 2014]. It has been proposed that this feature of the TEC perturbations is related to the local magnetic field geometry [*Heki and Ping*, 2005; *Shinagawa et al.*, 2007]. Recent detailed simulations by *Zettergren and Snively* [2013] have confirmed that the geomagnetic field does induce significant anisotropy in TEC perturbations produced by a weather-related source of low-frequency acoustic waves which agree remarkably well with signatures reported by *Nishioka et al.* [2013].

Infrasonic-acoustic waves have been simulated as a response to compressions due to the thermal forcing associated with tropospheric weather [*Walterscheid et al.*, 2003] and gusty flow over terrain [e.g., *Walterscheid and Hickey*, 2005], predicting waves with periods of tens of seconds to several minutes propagating well into the mesosphere and lower thermosphere. Simulations directed toward investigating the observable signatures of acoustic waves have also been reported, for the hydroxyl airglow response [*Snively*, 2013], the effects on subionospheric very low frequency electromagnetic propagation [*Marshall and Snively*, 2014], and the coupled *F* region ionospheric response [*Zettergren and Snively*, 2013]. Results suggest that waves with compressional velocities ~10s–100s m/s can detectably perturb each system. These studies are in concurrence with recent and historic observations and confirm that these waves are readily detectable via contemporary optical and radio techniques; furthermore, they suggest new opportunities to improve the interpretations of observed signatures via modeling.

This paper extends the modeling work of *Zettergren and Snively* [2013] by investigating the ionospheric responses at a *range* of different magnetic latitudes to acoustic waves from *various* ground level or lower atmospheric sources. In particular, we model the impacts of idealized lower atmospheric sources (including a convective "storm" updraft, "volcano," and "earthquake" parameterized by vertical accelerations), which vary in temporal and spatial scale, at different locations. Our analyses of these simulations focus on both ionospheric density responses and the generation of detectable field-aligned currents, as well as observable quantities such as total electron content (TEC) and magnetic perturbations. The primary motivation of this study is to provide a set of results that illustrate the dependence of ionospheric responses on local magnetic field geometry and source geometric characteristics and intensities. Results provide example responses that can be compared against existing and future TEC, incoherent scatter radar (ISR), and magnetometer observations. They demonstrate the connection of source disturbance parameters (temporal and spatial scales, etc.) to observable frequencies and wavelengths present in TEC data. The production of ion sound waves in the topside ionosphere due to acoustic wave forcing is also investigated. Finally, our results are compared qualitatively to published examples of TEC and magnetometer perturbations from earthquakes, volcanoes, and weather sources.

Only a limited range of solar and geomagnetic conditions are considered for the model runs presented in this work (all simulations are for solar maximum, around noontime). Moreover, our models consider only the portion of the lower atmospheric forcing spectrum which excites waves that propagate into the thermosphere (roughly 1–4 min periods). Hence, this set of results is not comprehensive, nor are the simulations intended to model the response to any particular geophysical event. However, comparisons of these simulations with TEC and magnetometer data suggest that most features of the modeled ionospheric responses are indeed qualitatively consistent, thus enabling future detailed comparisons between model and data.

## 2. Modeling Approach

A set of two models is used to simulate the ionospheric response to ground level perturbations: (1) A neutral dynamics model based on *Snively and Pasko* [2008] is used to simulate atmospheric dynamics, viz., acoustic and gravity wave generation, propagation, and dissipation in the lower thermosphere; and (2) a comprehensive ionospheric model based on *Zettergren and Semeter* [2012], which encapsulates the ionospheric response to neutral forcing through neutral drag, dynamo currents, and modifications to thermospheric densities.

In addition to the usual atmospheric and ionospheric state parameters (mass, momentum, and energy densities) these coupled models also produce estimates of TEC and magnetic field perturbations due to acoustic waves generated by geologic and weather events. *Zettergren and Snively* [2013] demonstrates a similar use of these models under a much narrower range of locations and conditions. Although these models have been documented elsewhere, i.e., by *Snively and Pasko* [2008] and *Zettergren and Semeter* [2012], several components have changed in significant ways since they were originally reported. Therefore, descriptions of these models in their present forms, in a consistent notation, are provided in appendices, and a brief overview is included in this section.

### 2.1. Atmospheric Dynamics Model

Our neutral atmospheric dynamics model (described in detail in section A1) is a variant of that described by *Snively and Pasko* [2008] and *Snively* [2013]. It solves the Euler equations in conservation law form using a finite volume method based on LeVeque's "f-wave" approach [*LeVeque*, 1997; *Bale et al.*, 2002; *LeVeque*, 2002]. It is coupled with solutions for molecular viscosity and thermal conduction. The model can describe the nonlinear propagation of acoustic and gravity wave packets in an atmosphere with realistic winds, thermal structure, and composition, at finite amplitudes up to the onset of breaking (here limited by 2-D assumptions). The ambient atmospheric states for the neutral dynamics model are specified via NRLMSISE00 [e.g., *Picone et al.*, 2002], defining the composition, mass density, and temperatures. Winds are necessarily precluded by our cylindrically axisymmetric geometry; for simulations of vertically propagating acoustic waves, this assumption appears quite reasonable [e.g., *Snively*, 2013] as wave phase velocities are principally perpendicular to, and a factor of 10 larger than, typical horizontal wind velocities.

### 2.2. Ionospheric Model

The 2-D ionospheric model (described in detail in section A2) used in this study is based on the model developed in *Zettergren and Semeter* [2012] and later extended in *Zettergren and Snively* [2013] and *Zettergren et al.* [2014]. This model comprises a fluid system of equations [*Schunk*, 1977; *Blelly and Schunk*, 1993; *Huba et al.*, 2000a], describing dynamics of the ionospheric plasma, self-consistently coupled to an electrostatic treatment of auroral and neutral dynamo currents. The fluid system is a set of three conservation equations (mass, momentum, and energy) for each ionospheric species $s$ relevant to the $E$, $F$, and topside regions ($s = O^+, NO^+, N_2^+, O_2^+, N^+, H^+$). The ionospheric model makes use of a generalized orthogonal coordinate system, which implements, for the present study, a tilted dipole coordinate system [e.g., *Huba et al.*, 2000a].

### 2.3. Model Coupling and Configuration

The coupling of perturbations from the neutral dynamics model into the ionospheric model is achieved by using the atmospheric dynamics model to compute deviations from the empirical NRLMSISE00 atmospheres used in both models and inputting these deviations into the ionospheric model. Variations in $O$, $N_2$, $O_2$ density (solved via continuity equations each driven at the velocity of the major gas), temperature, and velocity components are considered in the simulations. The neutral perturbations factor into the ionospheric fluid system (equations (A7)–(A9)) through ion-neutral reactions/collisions and the electrostatic problem (equation (A14)) through the dynamo source term. Quantities are communicated between the models every 2 s, which requires an interpolation and rotation step to convert the neutral perturbations from their native geographic grid to the tilted dipole ionospheric grid. Figure 1 shows examples of the overlapping region of the two grids for the

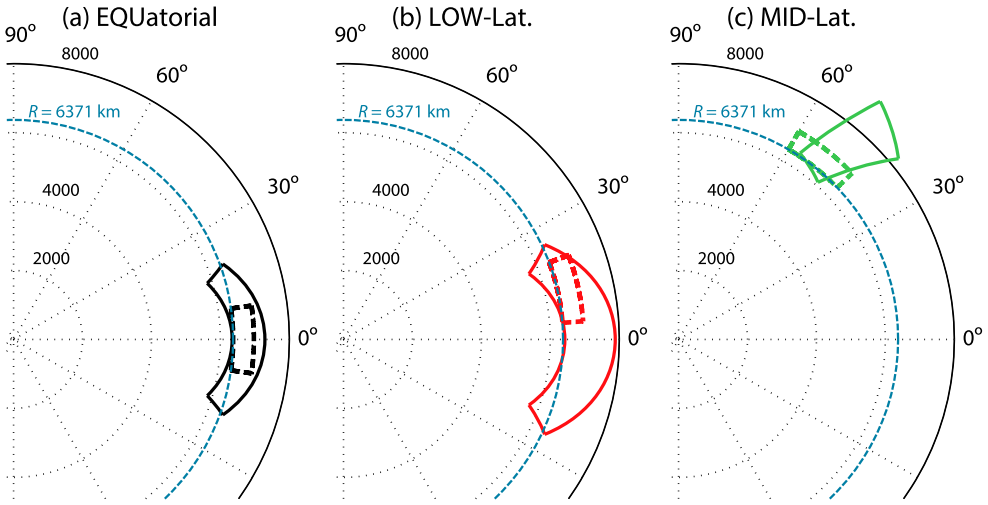


**Figure 1.** Model boundaries for the three different latitudes examined in this study (solid: ionospheric model, dashed: neutral dynamics model). The vertical direction in these plots represents the magnetic dipole axis. Hence, all latitudes are magnetic latitudes.

modeling cases presented in this paper. The solid lines in this figure represent the extent of the ionospheric grid, while the dashed lines indicate the limits of the neutral dynamics model. The neutral dynamics model uses a uniform mesh with grid spacing of 1 km and has an upper boundary of 600–700 km (depending on the type of wave that is simulated). The ionospheric mesh has variable grid spacing which decreases toward high altitudes (the spacing is ~1–5 km in the *E* and *F* regions). The upper boundary of the ionospheric model depends on the latitude (cf. Figure 1). For the grids used in this study it varies from ~900 to 3000 km in altitude.

Geographic locations for the simulations presented in this paper are listed in Table 1. Each of these locations is subjected to acoustic wave sources which approximate weather-related, volcanic, and seismic forcing described in section 3.1, thus resulting in nine total simulations. The geodetic longitude is fixed for each simulation so that the local time is essentially the same (approximately noon) for each (though the solar zenith angles and photoionization rates will vary due to latitude). The gap in grid latitudes between the low-latitude and mid-latitude cases is intentional; this region has, to a degree, already been examined in our previous study of tropospheric disturbance impacts on the ionosphere [*Zettergren and Snively*, 2013].

## 3. Responses of Atmosphere-Ionosphere System to Infrasound

### 3.1. Neutral Model Wave Sources

The neutral atmospheric dynamics model allows specification of initial conditions (leading to evolving dynamics) or time-dependent source terms, which can be constructed either analytically or based on modeled or measured input data. For the cases reported here, three sources are defined (Table 2) and then specified at three latitudes (Table 1). The sources are described by Gaussian accelerations of different spatial and temporal scales. They appear in the momentum equation as a "body force" term, proportional to density, $F_z = \rho A(r, z, t)$, and provide a vertical acceleration of Gaussian form:

$$A = A_0 \exp\left[-\frac{(r-r_0)^2}{2\sigma_r^2} - \frac{(z-z_0)^2}{2\sigma_z^2} - \frac{(t-t_0)^2}{2\sigma_t^2}\right], \quad (1)$$

**Table 1.** List of the Neutral Source Latitudes, Longitudes, Start Times, and Magnetic Latitudes

| | Latitude (deg) | Longitude (deg) | Start Time (UT) | Magnetic Latitude (deg) |
|---|---|---|---|---|
| EQUatorial | −10.39 | 270 | 18:00 | 0 |
| LOW-latitude | 2.08 | 270 | 18:00 | 12.44 |
| MID-latitude | 41.63 | 270 | 18:00 | 51.90 |

**Table 2.** List of the Neutral Source Forcing Parameters

| Source | $A_0$ | $\sigma_r$ (km) | $\sigma_z$ (km) | $\sigma_t$ (s) | $z_0$ (km) | $t_0$ (s) |
|---|---|---|---|---|---|---|
| Directive | 0.005 | 100 | 3 | 60 | 0 | 300 |
| Compact-60s | 0.125 | 5 | 3 | 60 | 12 | 300 |
| Compact-30s | 0.250 | 3 | 3 | 30 | 0 | 120 |

where $A_0$ is peak acceleration, $\sigma_r$ and $\sigma_z$ are horizontal and vertical half widths (standard deviations), respectively, and $\sigma_t$ is the temporal half width. It is positioned at $r_0 = 0$ km and $z_0$ is varied for each case; $t_0$ corresponds to the source maximum in time. Body force momentum sources have been used extensively to approximate the convective forcing of gravity waves [e.g., *Vadas*, 2013, and references therein].

These sources produce acoustic and also gravity waves with spectra similar to those routinely observed at *F* region altitudes above geophysical phenomena associated with natural hazard events. Although they do not describe the complete spectra generated by impulsive phenomena, they account for the observable fraction of the generated spectra, as indicated by the consistent ~1–4 min periodicities detected during natural hazard events (see section 1). This narrow band represents the dominant fraction of the spectrum that survives propagation through the dissipative, rarefied thermosphere.

The "Directive" source (Figure 2a) can be considered to approximate a vertical acceleration at ground level across a broad circular span, such as due to lifting of surface features during an earthquake or a sudden upward disturbance of the sea surface. Note that, alternatively, a downward acceleration could be specified, i.e., inverting the phase of the generated wave fields, or source could be defined on the basis of physical modeling. The most important feature of this model source, for purposes of comparison, is its directive radiation pattern, which produces nearly planar upward propagating acoustic waves in the ~3–4 min range. The structure of the wave appears nearly linear (minimal evidence of steepening).

The "Compact-60s" source (Figure 2b) approximates an updraft associated with strong convection, extending toward the tropopause, and has been used recently in modeling studies reported by *Snively* [2013] and *Zettergren and Snively* [2013], generating waves similar to those reported above tornado-producing storms, e.g., *Nishioka et al.* [2013]. It is spatially localized relative to the scales of generated acoustic waves; its radiation pattern is nearly spherical, producing acoustic waves in the ~3–4 min range. The wave exhibits mild steepening through the lower thermosphere (*E* region), where it is also refracted and gradually reflected; these features are due in part to spherical geometry and the angle of the wave relative to the thermospheric temperature gradients.

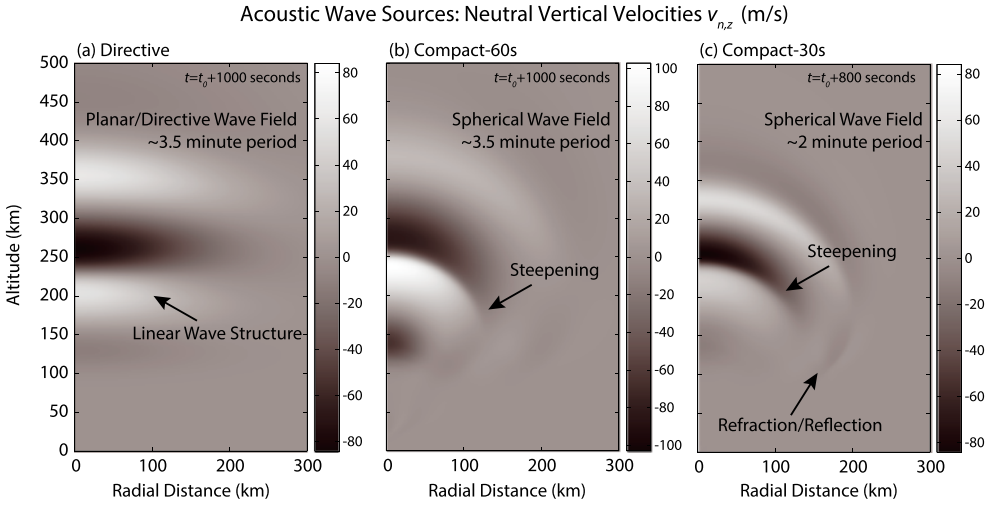


**Figure 2.** Neutral vertical velocities for each source at time 1000 s (or 800 s) after the source initiation ($t_0$ + 1000 s or ($t_0$ + 800 s) for the mid-latitude simulations. Panels depict the following: (a) Directive source; (b) Compact-60s source; and (c) Compact-30s source. Note annotations indicating refracted/reflected waves, steepened features, and dissipative reduction of amplitude (and elimination of steepened features) at high altitudes.

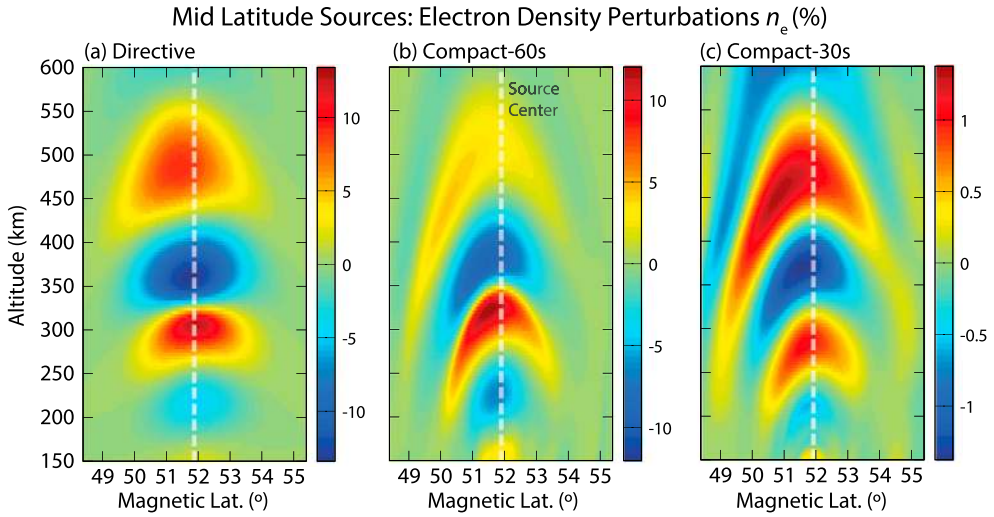


**Figure 3.** Electron density perturbations (percentage change from background) for each source at time 1300 s after the source initiation for the mid-latitude simulations. The magnetic latitude of the source perturbation is marked by a dashed line in each plot. Panels depict: (a) Directive source; (b) Compact-60s source; and (c) Compact-30s source.

The "Compact-30s" source (Figure 2c) approximates explosive venting at ground level above an active volcano and exhibits smaller spatial and shorter temporal scales. Alternatively, similar sources may appear in convective systems (i.e., updrafts exhibiting relatively shorter time scales). Like the "Compact-60s" source, it is also spatially compact relative to the wavelengths of the generated waves, producing a spherical wave field with dominant periodicities in the ~1–2 min range [e.g., *Heki and Ping*, 2005]. However, as a broadband source, spectral content also extends into the ~3–4 min range albeit at lower amplitudes. Similar to the "Compact-60s" waves, steepening and gradual refraction and reflection are seen in the lower thermosphere.

While acoustic waves presented in Figure 2 all have large wind velocities (> 80 m/s), direct measurements have revealed acoustic waves with velocities of ~130 m/s [*Garcia et al.*, 2013] following the Tohoku earthquake, even far from the epicenter. Moreover, qualitative comparison against TEC data in section 4 suggests that these acoustic waves have amplitudes consistent with those generated by realistic sources. Note, too, that the speed of sound is many hundreds of meters per second in the *E* and *F* regions, enabling nearly linear propagation of acoustic waves with compressional velocities even exceeding 100 m/s.

### 3.2. Ionospheric Densities

Figure 3 shows plots of the percent electron density perturbation for the mid-latitude simulations at a time when the acoustic wave has impacted the *F* region ionosphere ($t_0$ + 1300 s). The primary physical process responsible for creating these density perturbations is ion-neutral collisional momentum transfer. The wavefront shapes of the source acoustic waves are evident in the electron densities (i.e., planar phase structure for the Directive source and spherical for the others). The Directive and Compact-60s examples produce more pronounced effects (±12% density fluctuations) while the Compact-30s case is about a factor of 10 weaker (±1.2%).

A pronounced equatorward tilt to the density perturbations is present in each simulation. The acoustic waves have a perfectly symmetric radiation pattern (in the radial coordinate), so this feature is entirely due to the local magnetic field geometry effects on plasma transport. Specifically, at the *F* region altitudes both the ions and electrons are strongly magnetized, so the plasma moves most easily along the field line. Coupled with a stronger magnetic field-aligned neutral wind toward the magnetic south, this produces a preferential plasma motion toward the magnetic equator.

A particularly revealing feature in Figure 3 concerns the spatial scales of the Compact-30s source compared to those of the Directive and Compact-60s cases. At the lower altitudes shown in Figure 3 (e.g., ~220 km), the higher-frequency Compact-30s source clearly produces smaller-scale features in the electron density. However, above approximately 300 km, the dominant spatial scales are essentially the same as for the lower frequency Directive and Compact-60s sources. This behavior results from the strong dissipation of the

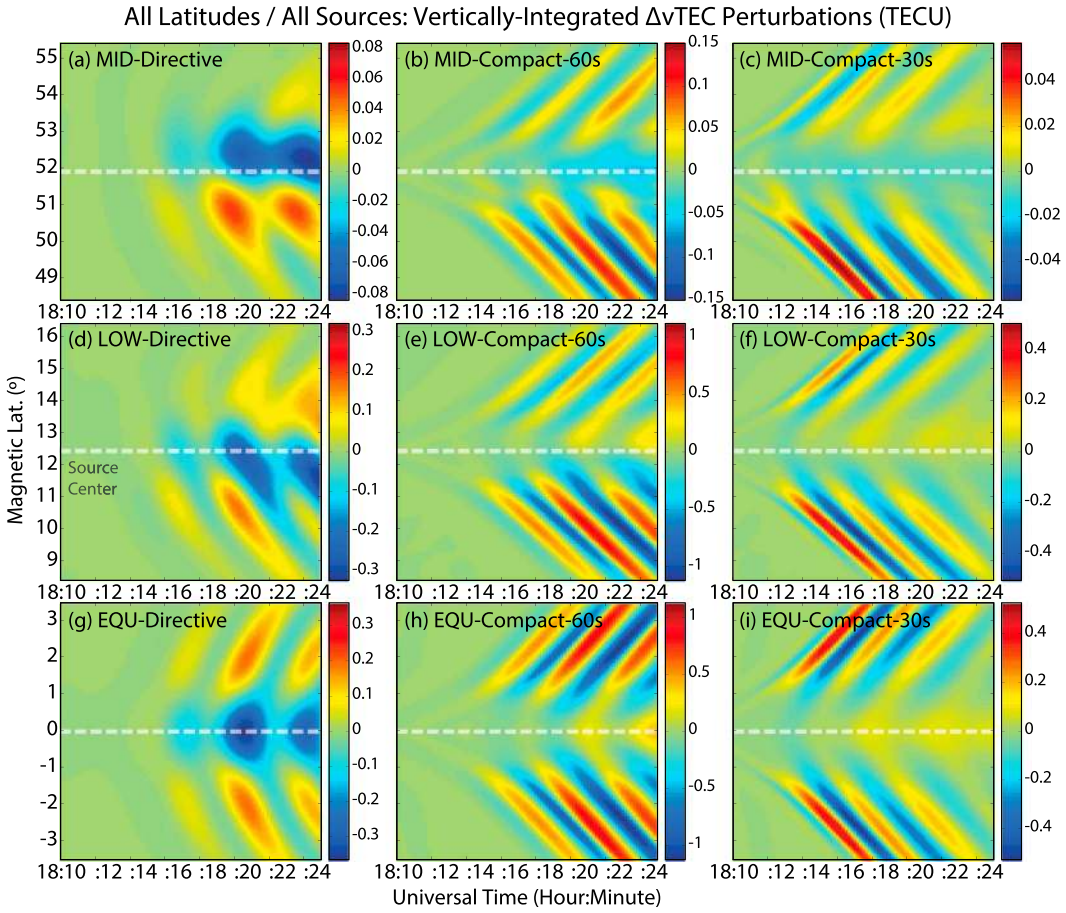


**Figure 4.** Total electron content perturbations (background subtracted) for each simulation (all sources initiated at 18 UT). Note the different color ranges for each. The magnetic latitude of the source perturbation is marked by a dashed line in each plot. Panels depict (a) mid-latitude, Directive; (b) mid-latitude, Compact-60s; (c) mid-latitude, Compact-30s; (d) low-latitude, Directive; (e) low-latitude, Compact-60s; (f) low-latitude, Compact-30s; (g) magnetic equator, Directive; (h) magnetic equator, Compact-60s; and (i) magnetic equator, Compact-30s.

higher-frequency wave components through the thermosphere. Thus, only longer-wavelength features, similar in scale to those produced by the Directive and Compact-60s sources, survive near the peak of the *F* region ionosphere. Dissipation also accounts for the fact that the density perturbations following the Compact-30s source are much smaller than those in the other cases.

### 3.3. GPS-Observable Impacts of Acoustic Waves: TEC Perturbations

Figure 4 shows the results for vertical TEC perturbations (TEC Units, TECU) versus time and magnetic latitude. As the simulations are specified for noontime, solar maximum conditions, these TEC perturbations likely represent the maximum attainable for the given sources. Indeed, *Zettergren and Snively* [2013] showed a strong dependence of the amplitude of TEC perturbations on photoionization (see their Figure 4). Their results show that an acoustic wave in a sunlit ionosphere (74° solar zenith angle, SZA) generates larger amplitude TEC perturbations (by about a factor of 3) than a similar acoustic wave source does in the conjugate ionosphere (which has SZA of 96°).

Figure 4 shows that all sources and latitudes exhibit detectable TEC perturbations and, for a given source, the TEC variations weaken with increasing magnetic latitude. This is at least partially due to the lower background densities present at the higher latitudes. Note that the simulated responses at the equator for all sources are symmetric, while for the higher latitudes there is always a stronger TEC response to the south. This anisotropy ranges between factors of roughly ~1.6–2 for the low-latitude and mid-latitude Compact-60s and Compact-30s cases.

**Table 3.** Major Periodicities (s) and Wavelengths (km) of Low-Latitude TEC Perturbations[a]

| | Directive | Compact-60s | Compact-30s |
|---|---|---|---|
| Period (s) | 200–240 | 168–200 | 155–200 |
| Wavelength (km) | 400 | 180–250 | 120–200 |

[a]Note that (1) all examples have long periodicities just near the source magnetic latitude and (2) all examples also have long wavelengths appearing at the later times.

TEC responses to waves generated by the Compact sources are similar in many respects, due to the associated waves being approximately spherical in form (due to having very long wavelengths relative to the radial scales of the sources). In particular, both types of sources produce TEC *phase structure* which is mirrored about the source location (i.e., symmetric about the source latitude). The largest perturbations are of the order of 1 TECU—larger by far than those of our Directive source and occur >0.5–1°away from the source location. Only a relatively small amplitude deviation is present near the source magnetic latitude, and this deviation is negative in the mid-latitude case (∼ −0.01 to −0.02 TECU) and positive at low and equatorial latitudes (∼0.15–0.2 TECU). The main difference between the 60s and 30s source cases is that the 60s source wave perturbations are larger by about a factor of 2 (due to dissipation of the higher-frequency waves associated with the faster source).

The Directive source responses are notably different from the other sources due to the planar phase structure. This manifests as TEC responses with longer periodicities and significant variations over the source latitude (marked as a dashed line in each figure). The Directive source is the only one that produces a relatively strong TEC response (i.e., close to maximum perturbation for the simulation) directly above the source location. In all cases the TEC response above the source is negative, ∼ −0.3 TECU maximum for the equator and low-latitude case and −0.08 TECU maximum for the mid-latitude case. For a given magnetic latitude, the Directive source always has the weakest TEC perturbations, even though the neutral velocities of its acoustic wave are either larger than or comparable to the other sources. This is likely due to a "Venetian Blind" effect caused by the directive source wavevectors being aligned with the vertical direction. Vertical integrations of electron density, for this type of wave configuration, include successive positive and negative density perturbation regions and partially cancel.

A spectral analysis of the TEC fluctuations for the low-latitude simulations is performed by separately taking discrete Fourier transforms of the model output in time and space. This results in a frequency spectrum versus magnetic latitude and a wave number spectrum versus time. The main results of these analyses are summarized in Table 3 and discussed below. Figures of the spectra are not presented, as most of the features discussed below can be discerned by careful inspection of Figure 4.

The Directive source's maximum TEC power appears just south (at ∼12.1° magnetic latitude) of the source location and is near the longest detectable periodicity. Another obvious spectral feature of ∼220 s period is present near 11.5° magnetic latitude (within a degree of the source). The Compact (60s and 30s) simulations have, in general, quite similar frequency spectral features (maximum power at periodicities of ∼185 and 175 s, respectively). For the Compact-30s simulation, the dominant periodicities show two maxima in their frequency spectra, a stronger peak around 10° magnetic latitudes and a somewhat lesser peak at around 15°. Each of these peaks corresponds to the main fluctuations seen to the north and south of the source in Figure 4f. A lower frequency (near the limit of what can be discerned from the model output), weaker spectral component exists centered around 11.5 and 12.75°, respectively. The spectral similarity between the 30s and 60s cases is, at least partially, another manifestation of the dissipation of the generated acoustic waves, which leaves mostly longer wavelengths and periods in the *F* region. The ∼1–2 min portion of the spectrum experiences more rapid damping, suggesting that time scales of events such as reported by *Heki and Ping* [2005] were shorter than those simulated.

Wavelength features for the three low-latitude simulations are also shown in Table 3. The Directive source has a dominant TEC perturbation wavelength of about ∼400 km, the Compact-60s source is 205 km, and the Compact-30s source is ∼160 km. There is a tendency in all of the wavelength spectra for the TEC fluctuations to start out near this dominant wavelength and for longer-wavelength components to appear at later times. This is a consequence of the bidirectionality of the TEC perturbations. Horizontal broadening of the TEC wave packet in the northward and southward directions adds longer-wavelength components to the spectra as time progresses.

**Table 4.** Apparent Phase Speeds (m/s) of TEC Perturbations Determined Graphically From Figure 4

| | Directive | Compact-60s | Compact-30s |
|---|---|---|---|
| MID-latitude | 1210 | 1000 | 970 |
| LOW-latitude | 1210 | 810 | 790 |
| EQUatorial | 1450 | 950 | 950 |

Apparent phase speeds of the simulated TEC fluctuations for each case are estimated graphically from Figure 4 and listed in Table 4. For all latitudes, the Directive source has the highest apparent phase speed (~1.25 km/s) by a significant margin. For the Compact sources, mid-latitude, and equatorial simulations the TEC perturbations have essentially identical speeds (~0.95 km/s). All phase speed values are comparable to thermospheric acoustic wave phase speeds. However, wave directivity (radiation pattern) obviously plays a role. In particular, for the Directive case, the large radius of curvature of the wave fronts causes the wave to pierce the *F* region ionosphere at similar times in regions that are separated by relatively large horizontal distances. This effect contributes to the larger apparent phase speed of the earthquake TEC perturbations (indeed, it exceeds the local thermospheric acoustic speed).

### 3.4. Dynamo Current Responses

Acoustic waves produced by the earthquakes, storms, and volcanoes (as approximated by the Directive, Compact-60s, and Compact-30s sources) generate dynamo currents in both the *E* and *F* regions of the ionosphere. Figure 5 shows examples of field-aligned currents (FACs) from each source, for the low-latitude simulations, during a time when the dynamo effects were fairly pronounced (~700–900 s, depending on the source timing). For all simulations the maximum field-aligned current (FAC) at these times was in excess of 0.1 $\mu A/m^2$. The Compact-60s source was the strongest at ~0.7 $\mu A/m^2$ peak, while waves generated by the Compact-30s and Directive sources produced weaker FAC responses (0.3 $\mu A/m^2$ peak and 0.15 $\mu A/m^2$ peak, respectively).

In general, the infrasound-generated field-aligned and field-perpendicular current densities fall into the $\pm 0.01-1$ $\mu A/m^2$ range. For quick reference, these intensities are several orders of magnitude lower than discrete auroral and equatorial electrojet currents, and within roughly an order of magnitude of *Sq* and region 1 and region 2 current systems [e.g., *Kelly*, 2009, and references therein].

For the Compact source cases, the largest FACs are produced to the north of the perturbation magnetic latitude. This feature results from the same process which results in enhanced TEC perturbations to the south; viz., the alignment of the acoustic wave velocity perturbations with the local geomagnetic field. In the case of density responses, the parallel component of the acoustic wave velocity is most important in effecting

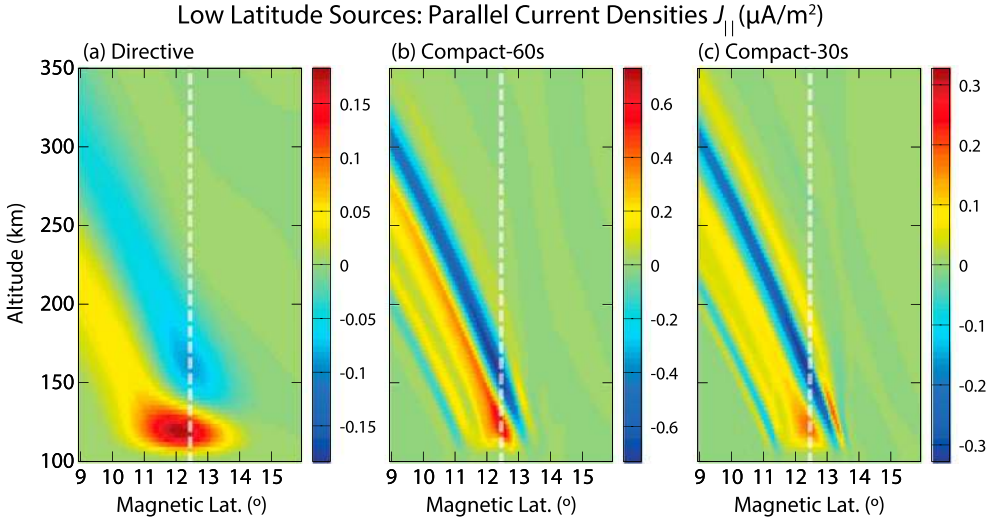


**Figure 5.** Field-aligned current for each source at time $t_0$ + 900 s ($t_0$ + 700 s for the Compact-30s case) for the low-latitude simulations. The magnetic latitude of the source perturbation is marked by a dashed line in each plot. Panels depict (a) Directive source; (b) Compact-60s source; and (c) Compact-30s source.

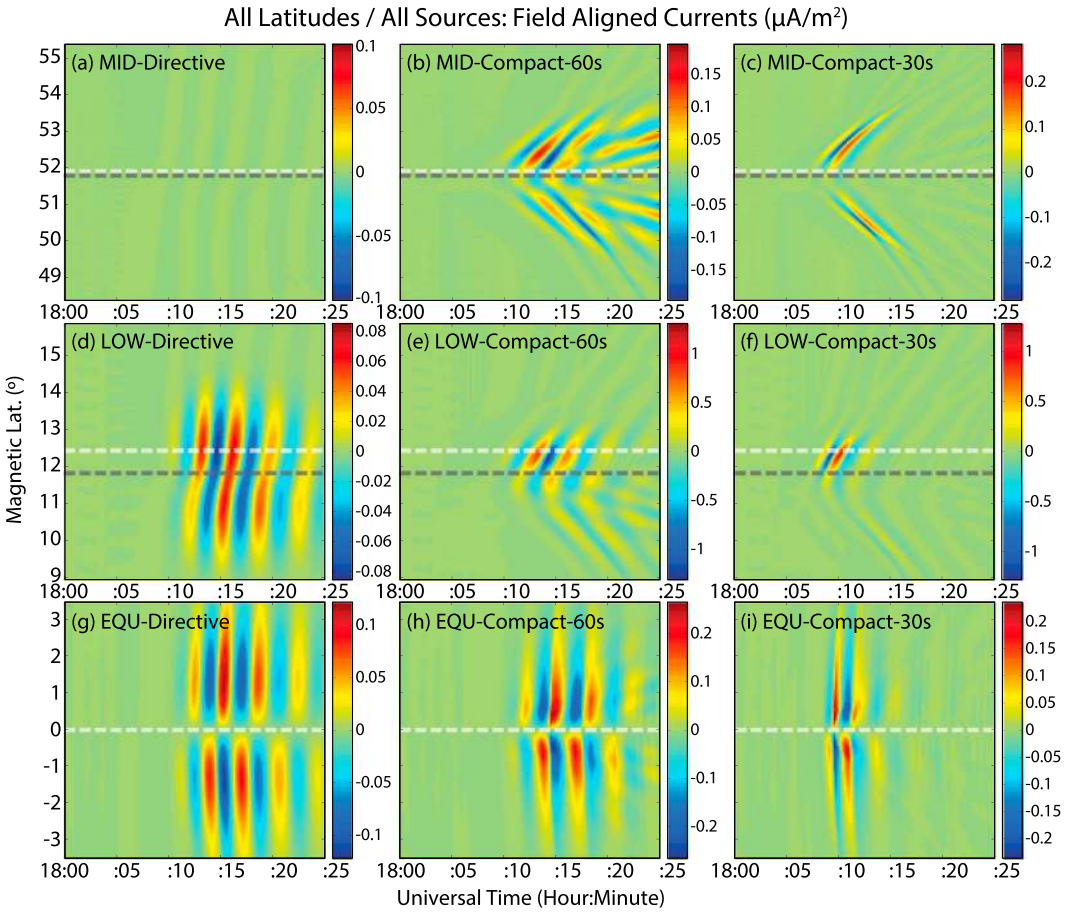


**Figure 6.** Dynamo field-aligned currents at 150 km for each of the nine simulations. Note the different color bar scales for each panel. The sign convention for these plots is positive along the field line (i.e., "downward" in the Northern Hemisphere, "upward" in Southern Hemisphere). For reference, the sources were initiated at 18 UT. The magnetic latitude of the source perturbation is marked by a light dashed line in each plot. The magnetic latitude of the field line at 150 km connecting to the dynamo region source location (assumed to be 120 km) is plotted as a dark dashed line. Panels depict (a) mid-latitude, Directive; (b) mid-latitude, Compact-60s; (c) mid-latitude, Compact-30s; (d) low-latitude, Directive; (e) low-latitude, Compact-60s; (f) low-latitude, Compact-30s; (g) magnetic equator, Directive; (h) magnetic equator, Compact-60s; and (i) magnetic equator, Compact-30s.

field-aligned plasma transport. For the electrodynamic responses, the perpendicular neutral wind components are the primary forcing mechanism (i.e., see the right-hand side of equation (A14)), which are indeed largest to the north of the source location. The Directive earthquake-like source is the lone exception and has its largest FAC perturbation directly above the source location.

Some small-scale structures are readily apparent near the horizontal edges of the FAC responses in the Compact source cases (see Figures 5b and 5c at ~120–140 km altitude near 13.3° magnetic latitude). These features are produced by refraction of the acoustic waves, evident in Figure 2, so that a larger geomagnetic perpendicular wind is present. The larger-scale FACs do partially map to higher altitudes (and the opposite hemisphere), but even so, quite a bit of current closure occurs in the source hemisphere. This can be most readily seen by examination of the 120–140 km region just above the sources in Figures 5b and 5c.

A final important point regarding Figure 5 is that a given FAC perturbation maps to lower magnetic latitudes as one follows a given magnetic field line upward in altitude. Hence, a current generated northward of the source latitude can map to a latitude south of the source when traced to higher altitudes. For example, in the low-latitude Compact-60s case in Figure 5b, the large negative FAC produced in the dynamo region (120–130 km altitude) is at approximately 13° magnetic latitude, but at an altitude of 250 km this FAC signature is at about 10.8°.

**Table 5.** Major Periodicities (s) and Wavelengths (km) of Low-Latitude Field-Aligned Current Perturbations

| | Directive | Compact-60s | Compact-30s |
|---|---|---|---|
| Period (s) | 200 | 168–200 | 90–150 |
| Wavelength (km) | >500 | 150–300 | 90–200 |

Summary plots of the field-aligned current responses versus time and magnetic latitude for each simulation are shown in Figure 6. These plots employ a cut in altitude at 150 km in the model. The light dashed line marks the magnetic latitude of the source, while the dark dashed line shows the magnetic latitude at 150 km which maps down to the dynamo region (nominally 120 km) above the source magnetic latitude. Note that the apparent FAC perturbation centers are the dark dashed lines in Figure 6. The most intense currents (up to ~1 $\mu A/m^2$) are generated by the Compact sources at low latitudes. The peak current for these sources at both middle and equatorial latitudes is only about a third of this value. For all latitudes the Directive source generates the weakest field-aligned currents. The mid-latitude Directive source, especially, produces a much smaller FAC response (~0.01 $\mu A/m^2$) than any of the other cases. Stronger FAC responses in the poleward direction (noted in Figure 5) are systematically present in the low-latitude and mid-latitude simulations driven by the Compact sources. For the cases where anisotropy is apparent it is much more pronounced at the low latitudes than at mid-latitudes.

A spectral analysis, similar to that employed for the TEC responses has been conducted with the FACs for the low-latitude simulations. Salient points of this analysis are summarized in Table 5 and discussed below.

The dominant FAC periodicities for the Directive and Compact-60s sources (~200 s for both) are similar to those found in the TEC analysis. In contrast, the Compact-30s (volcano-like) FACs have dominant power very close to the source periodicity as listed in Figure 2 (~120 s). This is notably different from the Compact-30s TEC perturbations which had significantly longer periodicities, ~180 s. This difference is attributable to the different altitudes which dominate the FAC versus TEC forcing. Specifically, the TEC response is most strongly controlled by the *F* region electron densities at altitudes where the high-frequency acoustic wave features are aggressively dissipated. In contrast, the FACs are dominated by the wave properties at dynamo region altitudes, around 120 km where dissipation is less important. Hence, higher-frequency wave components are important as dynamo sources even though they may not have corresponding TEC impacts. It is also worth noting that the Compact-30s source has significant power at periodicities (~90 s), below the expected linear source periodicity, associated with nonlinear wave steepening.

Wavelengths of the FAC perturbations roughly correspond with those of the TEC responses for the Compact source cases examined (~225 km and 145 km, respectively). The Directive FACs have very long-wavelength spectral content (>400 km, similar to the TEC wavelengths). In the Compact cases, there is a tendency for longer-wavelength features to develop at times later than when the major wavelength features appear. This is, again, attributable to the bidirectional nature of the FAC perturbations.

Currents and electric fields partially map to the opposite hemisphere, as illustrated here for the low-latitude cases. Figure 7 shows the $x_3$ component of the ion drift velocity at 200 km altitude. This zonal velocity is impacted by both local neutral wind drag and from electric fields, which induce an $\mathbf{E} \times \mathbf{B}$ drift (see equation (A11)). The electric field component of this drift will partially map to the opposite hemisphere. As with the current density, the light dashed lines mark the source magnetic latitude, while the dark lines mark the magnetic latitude at 200 km that maps to the dynamo region directly above the source. All of the simulated acoustic wave sources generate zonal drifts of the order of 1–5 m/s. These drifts are not particularly strong and seem unlikely to greatly affect densities in the source or conjugate hemispheres for the time scales considered here. As with the field-aligned current densities, the largest drifts in each case are northward of the mapped 200 km location of the perturbations (dark line). In the source hemisphere (northern), the drifts are larger due to the direct neutral wind effect, which also contributes relatively strong ion drift directly above the source location (light line).

### 3.5. Magnetic Field Perturbations

Magnetic perturbations due to "infrasound-driven dynamo" currents at $t_0 + 900$ s for the Compact-60s source, low-latitude simulation are shown in Figure 8. All components of the magnetic field perturbations near the current disturbances are in the ~2–15 nT range and may be detectable by satellite magnetometers under favorable conditions (low global geomagnetic activity levels). The signatures are not sustained, however, and

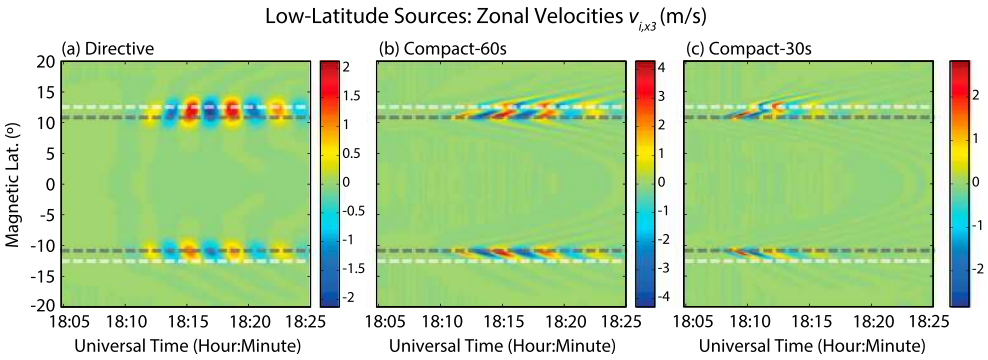


**Figure 7.** Zonal ion drifts induced by the acoustic wave in both the source and conjugate hemispheres for the low-latitude simulations for all sources. Dashed light lines and labels mark both the source (northern) hemisphere and conjugate (southern) hemispheres. The magnetic latitude of the field line at 200 km connecting to the dynamo region source location (assumed to be 120 km) is plotted as a dark line. Plots show evolution of the velocity at a fixed altitude, 200 km, versus magnetic latitude and time. Panels depict (a) low-latitude, Directive case; (b) low-latitude, Compact-60s case; (c) low-latitude, Compact-30s case.

are spatially localized, which may explain why few detections have been reported. The strongest field perturbations at ionospheric altitudes are in the zonal component (±15 nT). However, this component is very small below *E* region altitudes (~100 km) and does not have a large signature at ground. In contrast, vertical and meridional components have a maximum of about ±5 nT and ±8 nT, respectively, and have influence well below the ionosphere as seen in Figures 8a and 8b.

Ground level magnetic perturbations versus magnetic latitude have also been computed for each simulation. Results indicate that each of the sources create a similar signature in terms of spatial pattern and frequency so we present only the Compact-60s cases (the most intense). Figure 9 shows the results for vertical, meridional, and zonal magnetic field components at ground level versus magnetic latitude and time. All magnetic signatures commence at about 10 min into the simulation, which roughly corresponds to the acoustic wave travel time from the ground into the dynamo region. The strongest magnetic perturbations for each simulation are in the meridional component (~0.6–4 nT PTP, peak to peak), with the vertical component usually being about a factor of 2 smaller (~0.4–2.5 nT PTP). The vertical component perturbations are present at a wide range of latitudes (they span almost 10°) and switch direction, as expected, across the source latitude. In contrast, the meridional perturbations are much more localized (~5° wide) and are at a maximum at the source latitude. The zonal components are quite small (~0.1 nT PTP at most), but this may be a limitation of the sheet geometry assumed in calculating the magnetic fields (see section A2). The magnetic perturbations (all components) are largest in the equator simulation case and smallest in the mid-latitude case. Finally, in the low-latitude case, the vertical component has a very small, but noticeable conjugate magnetic perturbation at around ~15°. The amplitude of this conjugate fluctuation is about 0.2 nT PTP.

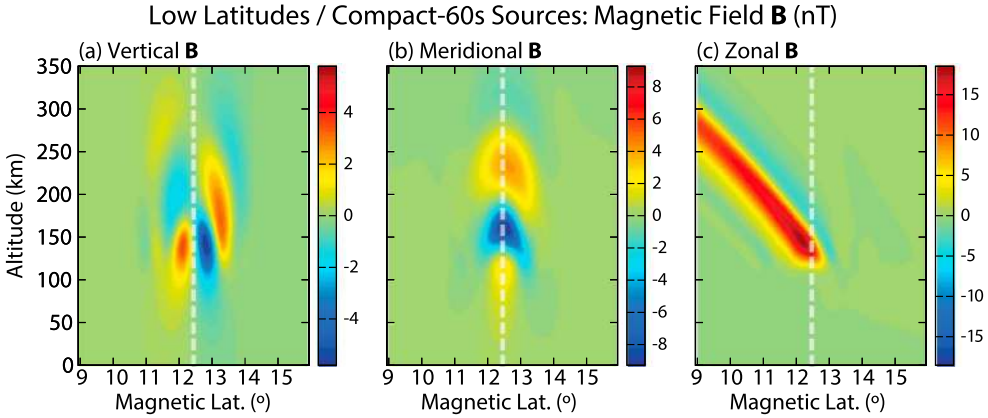


**Figure 8.** Magnetic field perturbations for the low-latitude Compact-60s simulation at $t_0$ + 900 s. Shown are the (a) vertical, (b) meridional, and (c) zonal components.

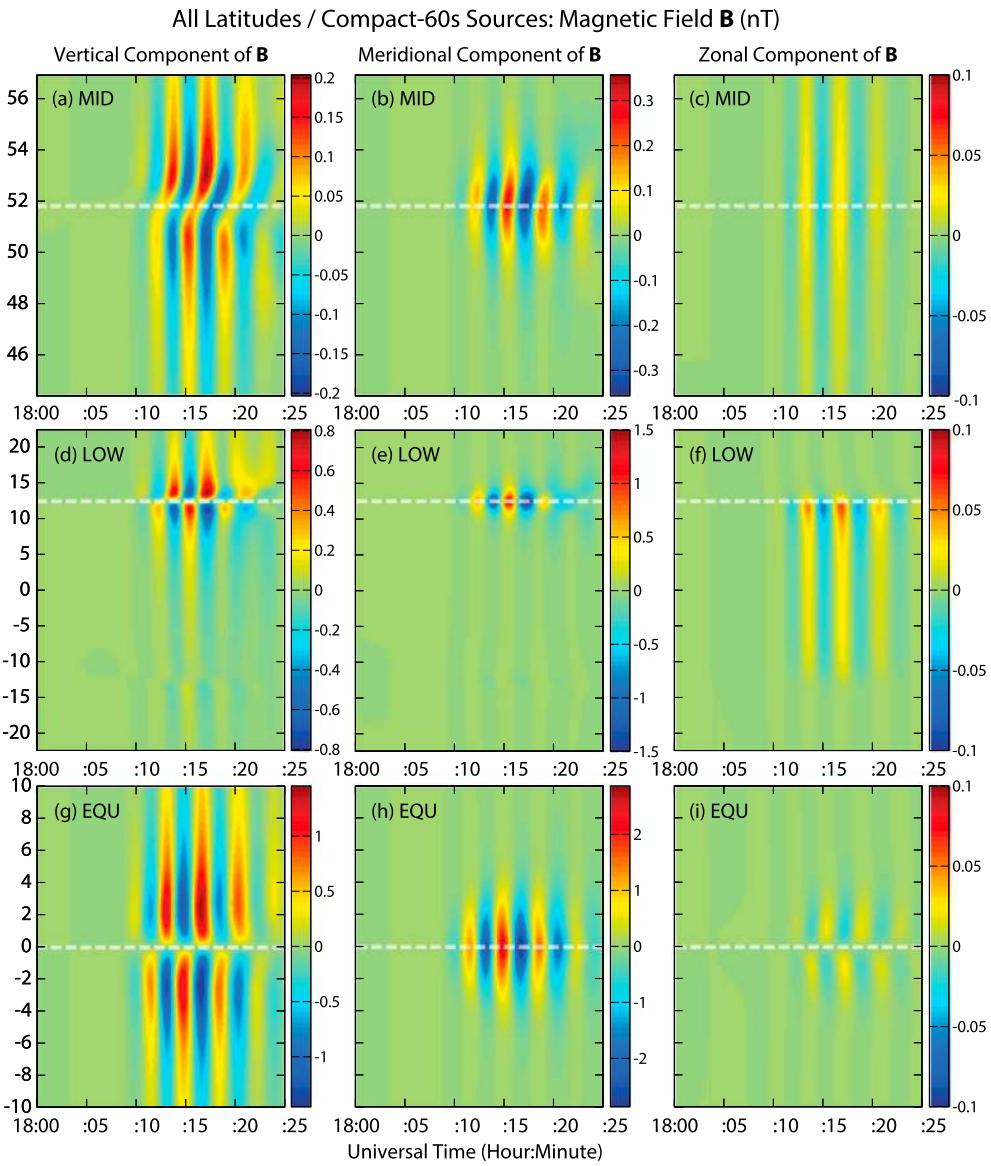


**Figure 9.** Ground-level magnetic field perturbations for the Compact-60s simulation versus time and magnetic latitude. Shown are the mid-latitude simulation (a) vertical, (b) meridional, and (c) zonal components; the low-latitude simulation (d) vertical, (e) meridional, and (f) zonal components; and the equatorial simulation (g) vertical, (h) meridional, and (i) zonal components.

### 3.6. Topside Ionospheric Impacts of Ground Level Events

The large-amplitude acoustic waves generated by all of our sources produce significant perturbations to the topside ionosphere, which persist even at altitudes where the acoustic waves have completely dissipated (>700 km). These topside disturbances propagate as ion sound waves [e.g., *Huba et al.*, 2000b], which are excited at and above the *F* region due to plasma density, temperature, and velocity disturbances. These high-altitude perturbations are demonstrated in Figure 10, which shows a snapshot of ionospheric and neutral atmospheric state variables at $t_0$ + 1500 s for the mid-latitude Directive simulation. Linear analysis of the topside fluctuations shown in Figure 10 confirms that these features propagate at the ion sound speed and that the pressure, density, and velocity fluctuations very nearly satisfy a linearized version of the ion fluid equations listed in section A2.

The wavelike structure of the plasma density (Figure 10a), temperature (Figure 10b), and velocity (Figure 10c) perturbations is consistent with that expected from a transition from a directly forced perturbation at the low altitudes to a freely propagating ion sound wave above ~600 km. Figure 10d shows the (neutral) velocity

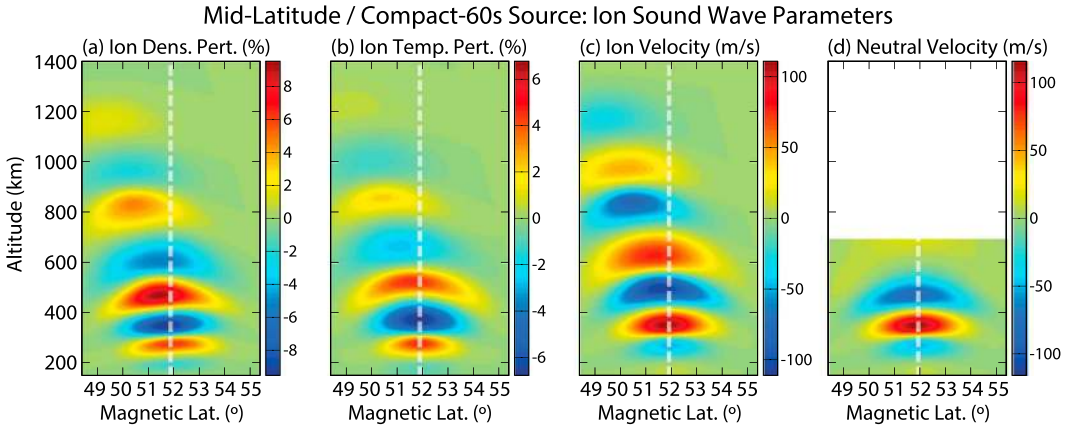


**Figure 10.** Perturbations to *F* region and topside ionospheric parameters for the mid-latitude Directive simulation 1500 s after source initiation. The magnetic latitude of the source perturbation is marked by a dashed line in each plot. (a) Percent electron density perturbations. (b) Percent ion temperature perturbations. (c) Ion velocity perturbations parallel to the geomagnetic field (positive "down"). (d) Neutral velocity perturbations parallel to the geomagnetic field.

of the acoustic wave. At the lower altitudes, phase structures in the ion state variables follow the neutral perturbation scale sizes. At higher altitudes, wavelength stretching of plasma state variables is apparent due to the higher-phase speed of the ion sound waves. The transition from a directly forced response to an ion sound wave (around 400–500 km altitude) also is marked by a slight change in wavevector direction. The plasma wave perturbations are guided by background geomagnetic field, so there is a tendency for the waves to turn southward above the altitude where they are generated. Amplitudes of the plasma parameter fluctuations maximize near *F* region altitudes at about 9% for density (Figure 10a), 6% for plasma temperature, and 50–100 m/s for velocity. At high altitudes (e.g., ~800 km), the ion sound wave amplitudes maximize at about 5% for density (Figure 10a), 2% for plasma temperature, and 75 m/s for velocity. Evolution of the ion sound waves with time is shown in Figure 11, which depicts the field-aligned neutral and plasma velocities along the centermost geomagnetic field line in the mid-latitude Directive simulation. The panels shown are times $t_0+1300$ (Figure 11a), $t_0+1400$ (Figure 11b), $t_0+1500$ (Figure 11c). The effects of viscosity on the neutral acoustic wave are apparent in these plots. The acoustic waves do steepen significantly through the 200 km region; however, the increase in acoustic speed through the lower thermosphere and increase in viscosity with decreasing density limit the effects of nonlinearity. Hence, the neutral perturbations retain minimal evidence of "steepness" above 400 km and are nearly dissipated by the time they reach 600 km. Consistent with the discussion above, the ion perturbations are in phase with the neutral acoustic wave up to about 400 km. As collisional coupling is significantly diminished at these altitudes and above, the faster ion sound wave propagates ahead of the source neutral disturbance, resulting in an apparent phase difference between ion and neutral species.

Mid-latitude Compact-30s and Compact-60s acoustic wave source simulations also show significant topside ionospheric perturbations. Ion sound waves are less efficiently excited by the Compact-30s source (±20 m/s), which produces waves that dissipate quite aggressively below the coupling region (~400 km) such that only weak longer-period waves remain. As a consequence of its omnidirectional radiation pattern, the longer-period Compact-60s source also excites a smaller ion sound wave than the Directive source. It tends to have lower velocity perturbations than the Directive source along the field lines; ion sound waves are, consequently, about 50% weaker (±45 m/s in the topside ionosphere).

Ion sound waves are identifiable in most of the low-latitude and mid-latitude simulations, but the Directive mid-latitude source produces the strongest ion sound wave signatures. The combination of the directive source and highly inclined geomagnetic field lines allows efficient coupling of neutral acoustic waves to plasma acoustic waves. Neutral velocities and acoustic phase structure are nearly aligned with the geomagnetic field and, thus, represent a partially coherent generator. The equatorial simulations do not appear to contain significant ion sound wave fluctuations (all of the perturbations are directly forced by ion-neutral drag). Some identifiable signatures of the ion sound wave do, however, appear in the low-latitude simulations, but they are very weak (velocity perturbations of ~5 m/s). The low amplitude of these cases is mostly due to

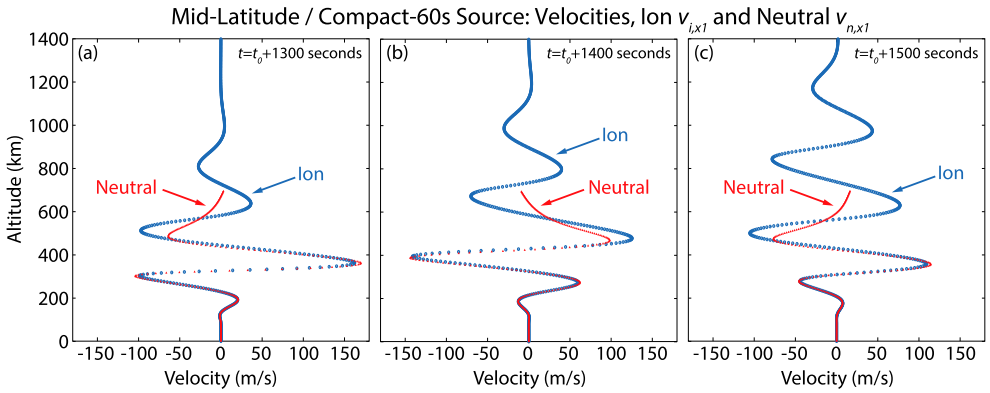


**Figure 11.** Perturbations to *F* region and topside neutral thermospheric and ionospheric drifts (neutral and ion sound waves, respectively) for the mid-latitude Directive simulation. The velocity profiles shown are the field-aligned components (positive "down") and are extracted along the center field line of the simulation. (a) Drift perturbations 1300 s after source initiation. (b) $t_0$ + 1400 s. (c) $t_0$ + 1500 s.

the longer path length of a field-aligned neutral ray through the dissipating region. Another contributing factor, in the case of the low-latitude Directive source, is that its radiation pattern is insufficiently aligned with the local magnetic field lines to generate a coherent ion sound wave perturbation.

The *F* region and topside density and velocity fluctuations are large enough that they may be detectable at mid-latitudes via high spatiotemporal resolution ISR experiment. A detailed investigation of their role in general atmosphere-ionosphere-magnetosphere coupling is unclear and beyond the scope of the present work.

## 4. Discussion

### 4.1. Consistency of Modeled TEC Responses With Observed Events

Simulated TEC perturbations due to the Directive (earthquake-like), Compact-60s (storm-like), and Compact-30s (volcano-vent-like) sources compare reasonably well with recently published accounts [*Tsugawa et al.*, 2011; *Saito et al.*, 2011; *Matsumura et al.*, 2011; *Nishioka et al.*, 2013; *Heki*, 2006]. It should be noted that the simulations have been set up without any attempt to match a particular event scenario and only approximate the observable fraction of natural hazard spectra. Hence, the comparisons that follow are intended to provide qualitative insight, to partially justify the choice of modeled infrasound sources and to identify opportunities for refinements toward future comprehensive case study modeling. A summary of events compared to our results is given in T able 6. These include the 2011 Tohoku earthquake, a 2013 EF5 tornado outbreak in Moore, OK, and the 2004 Asama volcano eruption in Japan.

Tohoku earthquake TEC responses [*Tsugawa et al.*, 2011; *Saito et al.*, 2011; *Matsumura et al.*, 2011] showed acoustic-wave-related features with periods of 222 s and peak-to-peak (PTP) oscillations of 0.5–1 TECU. As this event was during the daytime it is comparable to our Directive simulation cases, particularly the low-latitude and mid-latitude examples (the latitude of the Tohoku event, 38°N, was in between these two cases, but closer to mid-latitude). The TEC periodicities in our simulations (see Table 3) are very similar to those observed for Tohoku (~210 s). The maximum PTP amplitudes of the simulated TEC responses are 0.16 and 0.6 TEC for the mid-latitude and low-latitude cases, respectively. Several factors are likely causing the simulated mid-latitude TEC response (0.16 TECU) to be lower than that observed (>0.5 TECU). The first, noted above, is that the Tohoku latitude is at a lower latitude than that used in the mid-latitude simulation. An approximate conversion to the correct latitude would be to assume that the PTP model amplitudes, at the correct latitude, would be somewhere in between our middle- and low-latitude cases, perhaps ~0.3–0.4 TECU. This estimate is still weaker than the measured signatures; however, it appears likely that the Directive source used in the study was significantly weaker (perhaps by an order of magnitude) than the upward acceleration provided by the Tohoku earthquake (which had a 9.0 magnitude).

Though the simulated TEC responses show rough consistency with the data, several apparent features in the Tohoku earthquake event are not captured in our modeling. The 222 s periodicity is certainly present in the simulated TEC results (see Table 3) and is a consequence of the source periodicity and the tendency for shorter periods to be damped. However, our model has not been run long enough to investigate sustained TEC

**Table 6.** A Summary of Some Observed TEC Perturbations Following Seismic, Weather, and Volcanic Events

| Event | TEC PTP | $T$ (s) | $v_{ph}$ (m/s) | Location | Date[a] | Reference |
|---|---|---|---|---|---|---|
| Tohoku earthquake | 0.6 | 220 | multiple speeds present | Japan | 3/11/2011 05:46 UT (day) | *Saito et al.* [2011] |
| Moore EF5 tornado | 0.1–0.2 | 240 | 1300 | Oklahoma, USA | 5/20/2013 19:45 UT (day) | *Nishioka et al.* [2013] |
| Asama volcano | 0.16 | 75–100 | 1100 | Japan | 9/1/2004 11:02 UT (dusk) | *Heki* [2006] |

[a]Dates are formatted as month/day/year.

oscillations which lasted over half an hour after the earthquake [*Saito et al.*, 2011]. These persistent 222 s period oscillations have been attributed to an acoustic resonance in *Saito et al.* [2011] and *Matsumura et al.* [2011]. Another interesting feature, apparent in *Tsugawa et al.* [2011] and *Saito et al.* [2011], is the initial impulsive increase (~3 TECU) and then semipermanent decrease in the TEC (−4 TECU) marking the onset of the acoustic wave activity for the event. One speculation is that this feature is a nonlinear response to an initial acoustic shock wave. Our Directive source was not strong enough to generate a shock (see the rather linear wave features in Figure 2a). This again supports our assumption that the source amplitude is significantly lower than that of the Tohoku event; furthermore, the Tohoku forcing also included the simultaneous response of the ocean surface.

Statistical investigations of TEC measurements following earthquakes have been reported by *Perevalova et al.* [2014]. In particular, it was found that earthquakes of magnitude <6 appear undetectable in TEC data. The ~0.1 TEC signatures simulated for our Directive, mid-latitude case (Figure 4) appear likely consistent with a 7–8 magnitude earthquake. However, it is important to note that the ground perturbation associated with an earthquake exhibits greater complexity than a simple vertical acceleration at the surface (such as our "Directive" source models). *Astafyeva and Heki* [2009] note, too, ionospheric signature dependencies on the seismic disturbance, depending on the nature of the faults. Future theoretical and modeling studies can provide new insight into the response dependence on source characteristics.

An example of clear acoustic wave TEC features driven by a storm system is presented in *Nishioka et al.* [2013]. Following the May 2013 Moore, Oklahoma EF5 tornado, TEC perturbations identifiable with acoustic waves were observed. These oscillations had peak-to-peak amplitudes of 0.1–0.2 TECU and were notably stronger to the south. The acoustic wave-associated TEC perturbations also had a dominant periodicity of ~240 s and an apparent phase speed of 1.3 km/s (see Table 6 for details). The conditions under which this event occurred (mid-latitude, during the daytime) are similar to our Compact-60s stormlike simulations summarized in Figure 4b. The simulated TEC responses, indeed, are quite close to the values observed in *Nishioka et al.* [2013], having PTP amplitude of 0.24 TECU southward and 0.12 TECU northward (see Figure 4), 170–200 s major periodicities (Table 3), and apparent phase speed of ~1 km/s (Table 4). One slight difference between the model and this event appears to be the periodicities, which could easily be due to a difference in model source spectrum (~210 s). In the Moore event the acoustic-generated TEC oscillations continued for many hours after the onset and may indicate a persistent source in the troposphere or some type of acoustic resonance effect (or both) not examined in our shorter simulations.

In September 2004 the Asama volcano eruption in Japan generated significant TEC perturbations, which have been analyzed and documented in *Heki* [2006] and summarized in Table 6. Our mid-latitude Compact-30s case represents conditions most similar to this event, although the latitude is too high and the background solar flux too intense (these processes partially cancel each other in terms of their effects on TEC perturbations). Our simulation had peak-to-peak amplitudes of 0.12 TECU southward (see Figure 4) and 0.04 TECU northward, 155–200 s major periodicities (Table 3), and apparent phase speed of ~1 km/s (Table 4). The major difference in this case is the observed versus modeled periodicities (170 s versus 75–100 s). A shorter period source may be responsible for this difference, but such a source would radiate acoustic waves that dissipate more than those that we have modeled (which themselves dissipate rather aggressively). Hence, the actual Asama eruption source amplitude may also have been higher than that used in our model, likely also containing more energy at shorter periods.

### 4.2. Consistency of Modeled Magnetic Field Responses With Observed Events

While the TEC responses to natural hazard events have been fairly well-documented, measurements and analysis of magnetic fluctuations and ionospheric currents are less commonly subjected to detailed analysis. Several studies have attempted in situ detection of field-aligned currents generated by natural hazard events.

For example, *Balasis and Mandea* [2007] examined CHAMP magnetometer measurements during the 2005 Sumatran earthquakes and did not detect a disturbance which could unambiguously be related to the earthquakes. However, recently [*Iyemori et al.*, 2015] detected small-scale magnetic perturbations at frequencies indicating that the source could be "an infrasound-driven dynamo."

Ground-based magnetometer measurements from Sumatran [*Hasbi et al.*, 2009; *Iyemori et al.*, 2005] and Tohoku earthquake events [*Hao et al.*, 2012] appear to show convincing evidence for sizable dynamo currents associated with acoustic perturbations from these earthquakes. In particular, magnetometer infrasound-frequency fluctuations are roughly delayed from the earthquake occurrence time by the acoustic wave travel time to the *E* region ionosphere, just as in our simulations. Ground magnetic field fluctuations from observed events tend to be in the 0.1 – 1 nT peak-to-peak amplitude range in all geographic components. Our simulation results fall into this range and are even a bit larger in some cases (see Figures 9d, 9e, 9g, and 9h). Overestimates in our calculations may be due to the fact that the detections have been away from the epicenters of the earthquake or could be due to our use of planar geometry in magnetic field calculations.

### 4.3. Model Assumptions and Future Extensions

Results presented in this paper and comparisons with existing data give a strong indication that the model properly simulates TEC and magnetic fluctuations due to infrasound forcing of the ionosphere. Nevertheless, there are several assumptions used in our present modeling, discussed below, which indicate important opportunities for extensions in future related work.

First, the atmospheric dynamics model assumes a Navier-Stokes description of viscosity at all altitudes and a high level of coupling such that all species share the same velocity. By ∼220 km, the mean free path approaches the grid scale resolution, and by the top of the domain the mean free path approaches the dominant acoustic wavelength. Although assumptions of a fluid continuum are tenuous at the highest altitudes within the domain, it is important to note that for all simulations shown, the Knudsen number, as referenced to wave scale, is $\ll 1$ throughout the regions of strong coupling near the *F* region peak. Furthermore, atomic oxygen is the dominant neutral species throughout the thermosphere, such that our viscous stress tensor (equation (A5)), which neglects bulk viscosity, is a reasonable approximation. Nevertheless, richer treatments of the viscous stress and associated gas kinetics (beyond Navier-Stokes) may prove necessary for the dissipation of waves [e.g., *Conrad and Schunk*, 1979] particularly those exhibiting stronger nonlinearity and "steepness" at high altitudes. Gently steepened features are indeed apparent in the model (Figure 2), and the accurate modeling of their nonlinear propagation through a dissipative medium is important especially for quantitative interpretations of ground-based data [e.g., *Lonzaga et al.*, 2015].

Second, the coupling of the neutral dynamics and ionospheric models used in this study is "one way," which allows for computationally efficient simulations, such that ion-neutral drag forces and frictional heating calculated in our ionospheric model do not need to be fed back into the neutral dynamics model. This simplification is here justified by the fact that the neutral density in our simulations is always larger than the ion density for altitudes where strong acoustic wave-ionospheric coupling occurs. Hence, the primary physical impact of the neutral perturbations is to induce an ionospheric response, while the ionospheric impacts on the neutrals may be considered a small correction (here neglected). While appropriate for the present study, an opportunity exists to fully couple these models for studies of neutral perturbations driven by ionospheric processes.

Third, ionospheric modeling in this study also assumes a two-dimensional geometry, where modeled quantities are independent of the $x_3$ (zonal) coordinate. For ionospheric forcing by a cylindrically symmetry acoustic wave, this produces reasonably accurate results in the meridional plane of the acoustic wave source. Additionally, zonal drift structure also contributes to the density responses, but the computed zonal drifts appear fairly small (Figure 7) and in most situations would not be highly structured. The anisotropic and nonhomogeneous character of the conductivity in the ionosphere make it difficult to assess the impacts of the 2-D model assumptions on the simulated FACs, such that a 3-D treatment will provide further insight.

Aside from impacts on the density and FAC responses, a constraint imposed by the 2-D ionosphere is the manner in which the magnetic field perturbations are calculated, by assuming a current geometry that is infinite in $x_3$. As a result, the simulated magnetic field perturbations may be overestimated (and at least indicate a maximized result).

It is important to note that a fully 3-D treatment of the ionosphere at a physical level of detail achieved in this study presents a problem of enormous computational complexity (requiring $\sim 10^9$ grid points).

Relatively lower resolution 3-D simulations will be considered in the future, to further investigate the 3-D plasma response, magnetic field responses, and asymmetries of acoustic (and gravity) wave dispersion from realistic sources.

## 5. Conclusions and Future Work

This paper has presented a detailed, preliminary atmosphere-ionosphere modeling study of the impacts of ground level and lower atmospheric perturbations on the ionosphere, including electron and ion species density, field-aligned currents, and magnetic field responses. The models capture the dominant physical processes of the wave propagation and ionospheric response, such that simulated results appear directly comparable to recent GPS TEC and ground-based magnetometer observations. Sources and locations for our simulations have been chosen to specifically compare the impacts of local geomagnetic field geometry and source radiation pattern on observable responses of the atmosphere-ionosphere system.

All sources considered in this study produce waves that are easily detectable via GPS TEC measurements (>0.1 PTP TECU, Figure 4). The simulations indicate that larger TEC perturbations should be detected southward (equatorward) of the source, a result consistent with recently published observations [e.g., *Nishioka et al.*, 2013]. The stronger southward (equatorward) TEC perturbations should exist for all types of sources, unless they have a strong azimuthal dependence (a situation not considered in our studies). It is also possible that incoherent scatter radar could detect the ~10% electron density fluctuations and ±25–150 m/s drifts typical of these sources (Figure 3).

Directive sources lead to markedly different ionospheric response than do pointlike sources. The amplitudes of the TEC and FAC responses tend to be larger for the pointlike (spherical) sources (Figures 4 and 6)), while apparent phase speeds and wavelengths of TEC oscillations are larger for the more directive (planar, beamlike) sources (see Tables 3–5). The frequency content of TEC perturbations reveals only marginal information on source spectra, especially at shorter periods; indeed, most responses have dominant periodicities around 170–220 s, even if dominant source period is shorter (e.g., the Compact-30s simulations). This is a consequence of viscous dissipation of high-frequency, short-wavelength features at *F* region altitudes; the ~3–4 min features are those which remain intact and at moderately strong amplitudes.

Current densities excited by the acoustic waves are predicted to be quite large (>1 $\mu A/m^2$), particularly in the low-latitude Compact source cases (the nondirective sources, Figures 5b, 5c, 6e, and 6f). In general, it is also shown that field-aligned current (and magnetic field) perturbations contain higher frequencies than do the TEC responses. Indeed, the FACs are excited in the dynamo region (*E* region, nominally 120 km altitude), where viscous dissipation is much weaker. Steepening of the acoustic waves yields, in some cases (e.g., the volcano-vent Compact-30s source), higher frequencies (and thus smaller wavelengths) than present in parent source (see Table 5). The different spectral character of the excited field-aligned currents versus the density perturbations has implications for coupling with plasma wave modes. Tropospheric and ground-level acoustic wave sources will couple to different frequencies of Alfvén waves (which convey current along geomagnetic field lines) versus ion sound waves (which are excited from plasma density and pressure perturbations). Finally, the acoustic waves generate electric fields and zonal drifts which, while quite weak (approximately a few m/s), do map to the conjugate hemisphere and may have some impact.

Magnetic perturbations generated from dynamo currents in our simulations are predicted to exist and to be large enough to be detectable for all sources (i.e., "Directive," "Compact-60s," and "Compact-30s") at equatorial and low latitudes. Mid-latitude perturbations are weaker but may still be detectable in some cases. Small conjugate perturbations for low-latitude sources are predicted to exist.

Simulations presented in this paper provide a clear and detailed demonstration that ion sound waves can be excited by natural hazard sources. The excitation of these waves is most efficient in middle- to high-latitude regions where field lines and wavevectors are in approximately similar directions, and the acoustic ray path to *F* region ionosphere is small so that dissipation is minimized. Ion sound waves excited by the sources examined in this study are shown to be essentially linear and propagate freely through the topside ionosphere.

Most of the basic features of the simulated ionospheric responses are observationally consistent with recently published examples of ionospheric TEC responses to natural hazard events (see section 4.1). Cursory comparisons illustrate use of the modeling results presented in this paper to interpret existing data and reveal some

important differences. In particular, our results suggest that the Tohoku earthquake source was quite a bit larger than that used in the model and that the Asama volcano contained higher frequencies than the example sources used in this study. Furthermore, many observations have indicated sustained acoustic wave-related TEC signatures. Future detailed case studies and comparisons will be performed to investigate how source amplitudes, radiation patterns, and persistence may be inferred by using these models with existing GPS data.

Finally, this research has identified several areas that can benefit from further modeling and observations. A fully three-dimensional simulation is required to improve predictions of magnetic perturbations and to further investigate implications of the ion zonal drifts. Furthermore, the connection of acoustic wave-generated currents to ground level magnetic perturbations observed during earthquakes [*Iyemori et al.*, 2005; *Hasbi et al.*, 2009], including possible electrodynamic effects, should be investigated through more detailed case studies. Our preliminary comparisons reveal that more detailed data-model comparisons are likely to be quite fruitful, especially for sorting out the physical processes underlying the observed TEC perturbations during natural hazard events.

## Appendix A: Model Governing Equations

For reference, a description of the governing equations and numerical methods are provided for the neutral atmospheric dynamics and ionospheric models.

### A1. Neutral Atmospheric Model

The equations solved for the neutral dynamics model (see section 2.1) by the finite volume method of *LeVeque* [2002] are written in terms of conserved quantities mass density, momentum, and energy, with terms on the right-hand side accounting for dissipation (and departures from hyperbolic form):

$$\frac{\partial \rho}{\partial t} + \nabla \cdot (\rho \mathbf{v}) = 0 \tag{A1}$$

$$\frac{\partial}{\partial t}(\rho \mathbf{v}) + \nabla \cdot (\rho \mathbf{v}\mathbf{v} + p\mathbf{I}) = \rho \mathbf{g} + \nabla \cdot \boldsymbol{\tau} \tag{A2}$$

$$\frac{\partial E}{\partial t} + \nabla \cdot \{(E + p)\mathbf{v}\} = \rho \mathbf{g} \cdot \mathbf{v} + (\nabla \cdot \boldsymbol{\tau}) \cdot \mathbf{v} + \kappa \nabla^2 T \tag{A3}$$

In these equations **I** is the identity tensor. The energy equation and the equation of state for an ideal gas are defined as

$$E = \rho\epsilon + \frac{1}{2}\rho(\mathbf{v} \cdot \mathbf{v}) \qquad \epsilon = \frac{p}{(\gamma - 1)\rho} = \frac{k_B T}{m(\gamma - 1)} \tag{A4}$$

where $\rho$ is density, $p$ is pressure, $\mathbf{v}$ is the fluid velocity vector, $m$ is the mass per particle, $k_B$ is the Boltzmann constant, and T is the temperature; the energy density and specific internal energy density are given by $E$ and $\epsilon$, respectively. The viscous stress tensor is given by

$$\tau_{ij} = \mu \left( \frac{\partial v_i}{\partial x_j} + \frac{\partial v_j}{\partial x_i} - \frac{2}{3}\delta_{ij} \frac{\partial v_k}{\partial x_k} \right) \tag{A5}$$

The terms on the right-hand sides of the equations (1-3) are solved distinctly from the main hyperbolic system, with the exception of the terms accounting for gravity that are included via the f-wave approach [e.g., *Bale et al.*, 2002]. These terms account for a Navier-Stokes description of viscosity and conductivity and are applied using a time-split (fractional step) approach, where after each time step the velocity and temperature fields are derived from the conservative variables and passed into additional numerical solvers. Furthermore, solutions are included for terms arising from the cylindrically axisymmetric geometry used for the case studies considered here [e.g., *Snively*, 2013].

To allow use of efficient explicit methods, and to ensure stability, the time steps for all solvers are adaptive. Furthermore, two simplifying assumptions are made to improve computational efficiency. The viscous terms

in the momentum equation (A2) are solved neglecting the derivative of dynamic viscosity $\mu$ with altitude (which is indeed small), and in vector form can be written as

$$\frac{\partial}{\partial t}(\rho \mathbf{v}) + \nabla \cdot (\rho \mathbf{v}\mathbf{v} + p\mathbf{I}) = \rho \mathbf{g} + \mu \nabla^2 \mathbf{v} + \frac{\mu}{3}\nabla(\nabla \cdot \mathbf{v}) \tag{A6}$$

As an additional simplification of the conservative Navier-Stokes energy equation [e.g., *Landau and Lifshitz*, 1987, p. 193], although the redistribution of kinetic energy by viscosity is considered, the dissipation term $\boldsymbol{\tau} : \nabla \mathbf{v}$ is excluded from equation (A3), i.e., arising from $\nabla \cdot (\boldsymbol{\tau} \cdot \mathbf{v}) = (\nabla \cdot \boldsymbol{\tau}) \cdot \mathbf{v} + \boldsymbol{\tau} : \nabla \mathbf{v}$, as it is assumed small relative to the thermal conduction term.

### A2. Ionospheric Model

As discussed in section 2.2, the ionospheric model fluid system is a set of three conservation equations (mass, momentum, and energy) for each ionospheric species $s$ relevant to the $E$, $F$, and topside regions ($s = O^+, NO^+, N_2^+, O_2^+, N^+, H^+$).

$$\frac{\partial \rho_s}{\partial t} + \nabla \cdot \left(\rho_s \mathbf{v}_s\right) = m_s P_s - L_s \rho_s \tag{A7}$$

$$\left[\frac{\partial}{\partial t}\left(\rho_s \mathbf{v}_s\right) + \nabla \cdot \left(\rho_s \mathbf{v}_s \mathbf{v}_s\right)\right] \cdot \hat{\mathbf{e}}_1 = \left[-\nabla p_s + \rho_s \mathbf{g} + \frac{\rho_s}{m_s} q_s \mathbf{E} + \sum_t \rho_s \nu_{st}\left(\mathbf{v}_t - \mathbf{v}_s\right)\right] \cdot \hat{\mathbf{e}}_1 \tag{A8}$$

$$\frac{\partial}{\partial t}\left(\rho_s \epsilon_s\right) + \nabla \cdot \left(\rho_s \epsilon_s \mathbf{v}_s\right) = -p_s(\nabla \cdot \mathbf{v}_s) - \nabla \cdot \mathbf{h}_s - \frac{1}{(\gamma_s - 1)} \sum_t \frac{\rho_s k_B \nu_{st}}{m_s + m_t}\left[2(T_s - T_t) - \frac{2}{3}\frac{m_t}{k_B}(\mathbf{v}_s - \mathbf{v}_t)^2\right] \tag{A9}$$

The terms on the right-hand side of equation (A7) encapsulate chemical production and impact ionization ($P_s$) and chemical loss ($L_s$). Source terms in the continuity equation for photoionization are calculated according to the method presented in *Solomon and Liying* [2005] using solar fluxes from the EUVAC model [*Richards et al.*, 1994]. Impact ionization (not relevant to the present study) may be computed by one of several semiempirical methods based on *Semeter and Kamalabadi* [2005] and *Fang et al.* [2008, and references therein]. Chemical reactions for the ionospheric model are taken from *Diloy et al.* [1996] and *St.-Maurice and Laneville* [1998, and references therein]. In equation (A8) $q_s$ is the charge of each species, $\mathbf{v}_t$ is the drift velocity of species $t$ (which can be either charged or neutral), and $\nu_{st}$ is the collision frequency of charged species $s$ with species $t$. Note that the momentum equation (A8) is solved in a time-dependent form only for the direction parallel to the geomagnetic field (denoted by the unit vector $\hat{\mathbf{e}}_1$). The partial pressure $p_s$ is related to the specific internal energy by an equation of state (for each species) identical to that listed above for the neutral dynamics model (i.e., equation (A4)). The heat fluxes in equation (A9) ($\mathbf{h}_s$) are specified by a simple model of thermal conduction for the ions:

$$\mathbf{h}_s = -\lambda_s \nabla_{\parallel} T_s, \tag{A10}$$

where $\lambda_s$ is the thermal conductivity, taken from *Schunk* [1975]. Physical ion stresses are neglected in our model. For the perpendicular direction, a steady state momentum approximation is used:

$$\mathbf{v}_{s\perp} = \boldsymbol{\mu}_{s\perp} \cdot \left(\mathbf{E}_{\perp} + \frac{m_s \nu_s}{q_s}\mathbf{v}_{n\perp}\right). \tag{A11}$$

In this expression, $\boldsymbol{\mu}_{s\perp}$ is the ion mobility tensor and $\nu_s$ is the total ion-neutral collision frequency [*Zettergren and Semeter*, 2012]. A static geomagnetic field is used to compute the ion mobilities in equation (A11). Note that this steady state perpendicular drift assumption is consistent with the use of an electrostatic description for the fields, (cf. *Zettergren and Semeter* [2012], for a complete discussion).

Mass and momentum density state variables for the electron species are solved by invoking quasi neutrality and the definition of current density [cf. *Zettergren and Semeter*, 2012, equations (25) and (26)]. A full transport equation is solved for the electron energy.

$$\begin{aligned}\frac{\partial}{\partial t}\left(\rho_e \epsilon_e\right) + \nabla \cdot \left(\rho_e \epsilon_e \mathbf{v}_e\right) = -p_e(\nabla \cdot \mathbf{v}_e) - \nabla \cdot \mathbf{h}_e - \frac{1}{(\gamma_e - 1)} \sum_t \frac{\rho_e k_B \nu_{et}}{m_e + m_t}\Bigg[2(T_e - T_t) \\ -\frac{2}{3}\frac{m_t}{k_B}(\mathbf{v}_e - \mathbf{v}_t)^2\Bigg] + \frac{Q_e}{(\gamma_e - 1)}\end{aligned} \tag{A12}$$

For electron heat fluxes, both thermoelectric effects [*Schunk and Nagy*, 1978] and thermal conduction are considered [*Banks and Kockarts*, 1973a, 1973b; *Huba et al.*, 2000a]

$$\mathbf{h}_e = \left(-\lambda_e \nabla_\parallel T_e - \beta_e \mathbf{J}_\parallel\right). \tag{A13}$$

The electron energy equation also differs in form from the ion equation above (equation (A9)) in the inclusion of inelastic cooling terms and heating by photoelectrons, collectively denoted by $Q_e$. For the present work, cooling due to the excitation of rotational and vibrational modes of $O_2$ and $N_2$ are included, as is the excitation of fine structure of O. The photoelectron heating rate is calculated according to the method presented in *Swartz and Nisbet* [1972].

The electric fields needed for the momentum equation are found by using Ohm's law to specify current density and then invoking steady state current continuity and the electrostatic assumption, resulting in the following equation:

$$\nabla_\perp \cdot \left(\boldsymbol{\sigma}_\perp \cdot \nabla_\perp \Phi\right) + \nabla_\parallel \cdot \left(\sigma_0 \nabla_\parallel \Phi\right) = \nabla_\perp \cdot \left(\sum_s n_s m_s \nu_s \boldsymbol{\mu}_{s\perp} \cdot \mathbf{v}_{n\perp}\right). \tag{A14}$$

The usual expressions for Hall, Pedersen, and parallel conductivities are used in the solution of this equation. The assumptions inherent in the model equations (A7)–(A14) and numerical approaches have been discussed in detail in *Zettergren and Semeter* [2012]. Note, in particular, that we do not assume equipotential field lines in the solution for electric potential.

The two dimensions in the ionospheric model are along the field line ($x_1$) and in the direction of increasing L shell ($x_2$). All vectors have three components (i.e., they include a zonal, $x_3$, component), but they vary only in the $x_1$-$x_2$ plane.

Similar to the neutral dynamics model, a split time step procedure is used to separate equations (A7)–(A9) into advection, diffusion, and source/loss components. The advective parts of these equations are solved using a flux-limited finite volume method (MC flux limiter), the diffusion parts of the energy equations (encapsulating thermal conduction) are solved using a trapezoidal backward difference method (TRBDF2), and the source/loss parts are solved using either a Runge-Kutta method (for compression term in energy equation) or exponential time differencing scheme (for the remaining source terms, including collisions). A Von Neumann-Richtmyer artificial viscosity is used in the momentum and energy equations to prevent artifacts around steep features, but the simulations presented in this paper are not steep enough to be affected by this term. Lastly, equation (A14) is discretized using second-order, centered differences for the spatial derivatives. This produces a sparse system of equations for the electric potential, which is solved using the method and software described in *Davis* [2004].

The current densities obtained by solving equation (A14) are used to calculate magnetic field *perturbations* through the integral:

$$\mathbf{B}(\mathbf{x}) = \frac{\mu_0}{4\pi} \int \frac{\mathbf{J}(\mathbf{x}') \times (\mathbf{x} - \mathbf{x}')}{|\mathbf{x} - \mathbf{x}'|^3} d^3x', \tag{A15}$$

where the integration is performed using the model domain as the source coordinates ($\mathbf{x}'$) and a separate grid (which can be defined independent of model grid) for the field points ($\mathbf{x}$). Prior to evaluating equation (A15) all current densities are rotated into a local Cartesian coordinate system (with directions $x_{1,2,3}$ = up, south, and east) and the positions are also converted into local Cartesian coordinates. For purposes of calculating the integral in equation (A15), the currents are assumed to be infinite sheets in the zonal direction.

**Acknowledgments**
Research was supported by NASA grant NNX14AQ39G; generalized atmospheric and ionospheric models were developed by M.D. Zettergren and J.B. Snively under support from NSF CAREER grants AGS-1255181 and AGS-1151746, respectively, to Embry-Riddle Aeronautical University. Data appearing in plotted figures are available upon request.

Alan Rodger thanks two anonymous reviewers for their assistance in evaluating this paper.

## References

Artru, J., P. Lognonné, and E. Blanc (2001), Normal modes modelling of post-seismic ionospheric oscillations, *Geophys. Res. Lett.*, *28*(4), 697–700.

Astafyeva, E., and K. Heki (2009), Dependence of waveform of near-field coseismic ionospheric disturbances on focal mechanisms, *Earth Planets Space*, *61*, 939–943.

Baker, D. M., and K. Davies (1969), F2-region acoustic waves from severe weather, *J. Atmos. Terr. Phys.*, *31*, 1345–1352.

Balasis, G., and M. Mandea (2007), Can electromagnetic disturbances related to the recent great earthquakes be detected by satellite magnetometers?, *Tectonophysics*, *431*, 173–195, doi:10.1016/j.tecto.2006.05.038.

Bale, D. S., R. J. LeVeque, S. Mitran, and J. A. Rossmanith (2002), A wave propagation method for conservation laws and balance laws with spatially varying flux functions, *SIAM J. Sci. Comput.*, *24*, 955–978.

Banks, P. M., and G. Kockarts (1973a), *Aeronomy*, vol. A, Academic Press, New York.

Banks, P. M., and G. Kockarts (1973b), *Aeronomy*, vol. B, Academic Press, New York.
Blelly, P. L., and R. W. Schunk (1993), A comparative study of the time-dependent standard 8-, 13- and 16-moment transport formulations of the polar wind, *Ann. Geophys.*, *11*, 443–469.
Calais, E., and J. Bernard Minster (1995), GPS detection of ionospheric perturbations following the January 17, 1994, Northridge earthquake, *Geophys. Res. Lett.*, *22*(9), 1045–1048.
Conrad, J. R., and R. W. Schunk (1979), On the validity of the Navier-Stokes equations for thermosphere dynamics calculations, *J. Geophys. Res.*, *84*(A9), 5355–5360.
Dautermann, T., E. Calais, P. Lognonné, and G. S. Mattioli (2009a), Lithosphere-atmosphere-ionosphere coupling after the 2003 explosive eruption of the Soufriere Hills Volcano, Montserrat, *Geophys. J. Int.*, *179*, 1537–1546, doi:10.1111/j.1365-246X.2009.04390.x.
Dautermann, T., E. Calais, and G. S. Mattioli (2009b), Global Positioning System detection and energy estimation of the ionospheric wave caused by the 13 July 2003 explosion of the Soufrière Hills Volcano, Montserrat, *J. Geophys. Res.*, *114*, B02202, doi:10.1029/2008JB005722.
Davis, T. A. (2004), Algorithm 832: Umfpack v4.3—An unsymmetric-pattern multifrontal method, *ACM Trans. Math. Softw.*, *30*(2), 196–199, doi:10.1145/992200.992206.
Delclos, C., E. Blanc, P. Broche, F. Glangeaud, and J. L. Lacoume (1990), Processing and interpretation of microbarograph signals generated by the explosion of Mount St. Helens, *J. Geophys. Res.*, *95*(D5), 5485–5494.
Diloy, P.-Y., A. Robineau, J. Lilensten, P.-L. Blelly, and J. Fontanari (1996), A numerical model of the ionosphere, including the E-region above EISCAT, *Ann. Geophys.*, *14*, 191–200, doi:10.1007/s00585-996-0191-7.
Ding, F., W. Wan, T. Mao, M. Wang, B. Ning, B. Zhao, and B. Xiong (2014), Ionospheric response to the shock and acoustic waves excited by the launch of the Shenzhou 10 spacecraft, *Geophys. Res. Lett.*, *41*, 3351–3358, doi:10.1002/2014GL060107.
Fang, X., C. E. Randall, D. Lummerzheim, S. C. Solomon, M. J. Mills, D. R. Marsh, C. H. Jackman, W. Wang, and G. Lu (2008), Electron impact ionization: A new parameterization for 100 eV to 1 MeV electrons, *J. Geophys. Res.*, *113*, A09311, doi:10.1029/2008JA013384.
Galvan, D. A., A. Komjathy, M. P. Hickey, P. Stephens, J. B. Snively, Y. T. Song, M. D. Butala, and A. J. Mannucci (2012), Ionospheric signatures of Tohoku-Oki tsunami of March 11, 2011: Model comparisons near the epicenter, *Radio Sci.*, *47*, RS4003, doi:10.1029/2012RS005023.
Garcia, R. F., S. Bruinsma, P. Lognonné, E. Doornbos, and F. Cachoux (2013), GOCE: The first seismometer in orbit around the Earth, *Geophys. Res. Lett.*, *40*, 1015–1020, doi:10.1002/grl.50205.
Georges, T. M. (1973), Infrasond from convective storms: Examining the evidence, *Rev. Geophys.*, *11*(3), 571–594.
Hao, Y. Q., Z. Xiao, and D. H. Zhang (2012), Multi-instrument observation on co-seismic ionospheric effects after great Tohoku earthquake, *J. Geophys. Res.*, *117*, A02305, doi:10.1029/2011JA017036.
Hasbi, A. M., M. A. Momani, M. A. Mohd Ali, N. Misran, K. Shiokawa, Y. Otsuka, and K. Yumoto (2009), Ionospheric and geomagnetic disturbances during the 2005 Sumatran earthquakes, *J. Atmos. Sol. Terr. Phys.*, *71*, 1992–2005, doi:10.1016/j.jastp.2009.09.004.
Heki, K. (2006), Explosion energy of the 2004 eruption of the Asama Volcano, central Japan, inferred from ionospheric disturbances, *Geophys. Res. Lett.*, *33*, L14303, doi:10.1029/2006GL026249.
Heki, K., and J. Ping (2005), Directivity and apparent velocity of the coseismic ionospheric disturbances observed with a dense GPS array, *Earth Planet. Sci. Lett.*, *236*(3–4), 845–855.
Hines, C. O. (1972), Gravity waves in the atmosphere, *Nature*, *239*, 73–78.
Huba, J. D., G. Joyce, and J. A. Fedder (2000a), SAMI2 is another model of the ionosphere (SAMI2): A new low-latitude ionosphere model, *J. Geophys. Res.*, *105*, 23,035–23,054, doi:10.1029/2000JA000035.
Huba, J. D., G. Joyce, and J. A. Fedder (2000b), Ion sound waves in the topside low latitude ionosphere, *Geophys. Res. Lett.*, *27*, 3181–3184, doi:10.1029/2000GL003808.
Iyemori, T., et al. (2005), Geomagnetic pulsations caused by the Sumatra earthquake on December 26, 2004, *Geophys. Res. Lett.*, *32*, L20807, doi:10.1029/2005GL024083.
Iyemori, T., K. Nakanishi, T. Aoyama, Y. Yokoyama, Y. Koyama, and H. Luhr (2015), Confirmation of existence of the small-scale field-aligned currents in middle and low latitudes and an estimate of time scale of their temporal variation, *Geophys. Res. Lett.*, *42*, 22–28, doi:10.1002/2014GL062555.
Kelly, M. C. (2009), *The Earth's Ionosphere: Plasma Physics and Electrodynamics*, 2nd ed., Academic Press, New York.
Landau, E. M., and E. M. Lifshitz (1987), *Fluid Mechanics*, 2nd ed., Pergamon Press, New York.
Lay, E. H., and X.-M. Shao (2011), High temporal and spatial-resolution detection of D-layer fluctuations by using time-domain lightning waveforms, *J. Geophys. Res.*, *116*, A01317, doi:10.1029/2010JA016018.
LeVeque, R. J. (1997), Wave propagation algorithms for multidimensional hyperbolic systems, *J. Comp. Phys.*, *131*, 327–353.
LeVeque, R. J. (2002), *Finite Volume Methods for Hyperbolic Problems*, Cambridge Univ. Press, Cambridge, U. K.
Liu, C. H., et al. (1982), Global dynamic responses of the atmosphere to the eruption of Mount St. Helens on May 18, 1980, *J. Geophys. Res.*, *87*(A8), 6281–6290.
Liu, J.-Y., C.-H. Chen, C.-H. Lin, H.-F. Tsai, C. H. Chen, and M. Kamagawa (2011), Ionospheric disturbances triggered by the 11 March 2011 m9.0 Tohoku earthquake, *J. Geophys. Res.*, *116*, A06319, doi:10.1029/2011JA016761.
Lonzaga, J. B., R. M. Waxler, J. D. Assink, and C. L. Talmadge (2015), Modelling waveforms of infrasound arrivals from impulsive sources using weakly non-linear ray theory, *Geophys. J. Int.*, *200*(3), 1347–1361.
Makela, J. J., et al. (2011), Imaging and modeling the ionospheric airglow response over Hawaii to the tsunami generated by the Tohoku earthquake of 11 March 2011, *Geophys. Res. Lett.*, *38*, L00G02, doi:10.1029/2011GL047860.
Marshall, R. A., and J. B. Snively (2014), Very low frequency subionospheric remote sensing of thunderstorm-driven acoustic waves in the lower ionosphere, *J. Geophys. Res. Atmos.*, *119*, 5037–5045, doi:10.1002/2014JD021594.
Maruyama, T., T. Tsugawa, H. Kato, A. Saito, Y. Otsuka, and M. Nishioka (2011), Ionospheric multiple stratifications and irregularities induced by the 2011 Tohoku earthquake, *Earth Planets Space*, *63*(7), 869–873, doi:10.5047/eps.2011.06.008.
Matsumura, M., A. Saito, T. Iyemori, H. Shinagawa, T. Tsugawa, Y. Otsuka, M. Nishioka, and C. H. Chen (2011), Numerical simulations of atmospheric waves excited by the 2011 off the Pacific coast of Tohoku earthquake, *Earth Planets Space*, *63*(7), 885–889, doi:10.5047/eps.2011.07.015.
Nishioka, M., T. Tsugawa, M. Kubota, and M. Ishii (2013), Concentric waves and short-period oscillations observed in the ionosphere after the 2013 Moore EF5 tornado, *Geophys. Res. Lett.*, *40*, 5581–5586, doi:10.1002/2013GL057963.
Occhipinti, G. A., P. Coïsson, J. J. Makela, S. Allgeyer, E. Alam Kherani, H. Hébert, and P. Lognonne (2011), Three-dimensional numerical modeling of tsunami-related internal gravity waves in the Hawaiian atmosphere, *Earth Planets Space*, *63*(7), 847–851, doi:10.5047/eps.2011.06.051.
Perevalova, N. P., V. A. Sankov, E. I. Astafyeva, and A. S. Zhupityaeva (2014), Threshold magnitude for ionospheric TEC response to earthquakes, *J. Atmos. Sol. Terr. Phys.*, *108*, 77–90.

Picone, J. M., A. E. Hedin, D. P. Drob, and A. C. Aikin (2002), NRLMSISE-00 empirical model of the atmosphere: Statistical comparisons and scientific issues, *J. Geophys. Res.*, *107*(A12), 1468, doi:10.1029/2002JA009430.

Pilger, C., C. Schmidt, and M. Bittner (2013a), Statistical analysis of infrasound signatures in airglow observations: Indications for acoustic resonance, *J. Atmos. Sol. Terr. Phys.*, *93*, 70–79, doi:10.1016/j.jastp.2012.11.011.

Pilger, C., C. Schmidt, F. Streicher, S. Wüst, and M. Bittner (2013b), Airglow observations of orographic, volcanic, and meteorological infrasound signatures, *J. Atmos. Sol. Terr. Phys.*, *104*, 55–66, doi:10.1016/j.jastp.2013.08.008.

Richards, P. G., J. A. Fennelly, and D. G. Torr (1994), EUVAC: A solar EUV flux model for aeronomic calculations, *J. Geophys. Res.*, *99*, 8981–8992, doi:10.1029/94JA00518.

Roberts, D. H., J. A. Klobuchar, P. F. Fougere, and D. H. Hendrickson (1982), A large-amplitude traveling ionospheric disturbance produced by the May 18, 1980, explosion of Mount St. Helens, *J. Geophys. Res.*, *87*(A8), 6291–6301.

Rolland, L. M., P. Lognonne, E. Astafyeva, and E. Alam Kherani (2011), The resonant response of the ionosphere imaged after the 2011 off the Pacific coast of Tohoku earthquake, *Earth Planets Space*, *63*(7), 853–857, doi:10.5047/eps.2011.06.020.

Saito, A., T. Tsugawa, Y. Otsuka, M. Nishioka, T. Iyemori, M. Matsumura, S. Saito, C. H. Chen, Y. Goi, and N. Choosakul (2011), Acoustic resonance and plasma depletion detected by GPS total electron content observations after the 2011 off the Pacific coast of Tohoku Earthquake, *Earth Planets Space*, *63*, 863–867, doi:10.5047/eps.2011.06.034.

Schunk, R. W. (1975), Transport equations for aeronomy, *Planet. Space Sci.*, *23*, 437–485.

Schunk, R. W. (1977), Mathematical structure of transport equations for multispecies flows, *Rev. Geophys.*, *15*, 429–445.

Schunk, R. W., and A. F. Nagy (1978), Electron temperatures in the F region of the ionosphere: Theory and observations, *Rev. Geophys.*, *16*, 355–399.

Semeter, J., and F. Kamalabadi (2005), Determination of primary electron spectra from incoherent scatter radar measurements of the auroral E region, *Radio Sci.*, *40*, RS2006, doi:10.1029/2004RS003042.

Shinagawa, H., T. Iyemori, S. Saito, and T. Maruyama (2007), A numerical simulation of ionospheric and atmospheric variations associated with the Sumatra earthquake on December 26, 2004, *Earth Planets Space*, *59*, 1015–1026.

Snively, J. B. (2013), Mesospheric hydroxyl airglow signatures of acoustic and gravity waves generated by transient tropospheric forcing, *Geophys. Res. Lett.*, *40*, 4533–4537, doi:10.1002/grl.50886.

Snively, J. B., and V. P. Pasko (2008), Excitation of ducted gravity waves in the lower thermosphere by tropospheric sources, *J. Geophys. Res.*, *113*(A06303), doi:10.1029/2007JA012693.

Solomon, S. C., and Q. Liying (2005), Solar extreme-ultraviolet irradiance for general circulation models, *J. Geophys. Res.*, *110*, A10306, doi:10.1029/2005JA011160.

St.-Maurice, J.-P., and P. J. Laneville (1998), Reaction rate of $O^+$ with $O_2$, $N_2$, and NO under highly disturbed auroral conditions, *J. Geophys. Res.*, *103*, 17,519–17,522, doi:10.1029/98JA01387.

Swartz, W. E., and J. S. Nisbet (1972), Revised calculations of F region ambient electron heating by photoelectrons, *J. Geophys. Res.*, *77*, 6259, doi:10.1029/JA077i031p06259.

Tsugawa, T., A. Saito, Y. Otsuka, M. Nishioka, T. Maruyama, H. Kato, T. Nagatsuma, and K. T. Murata (2011), Ionospheric disturbances detected by GPS total electron content observation after the 2011 off the Pacific coast of Tohoku Earthquake, *Earth Planets Space*, *63*, 875–879, doi:10.5047/eps.2011.06.035.

Vadas, S. L. (2013), Compressible $f$-plane solutions to body forces, heatings, and coolings, and application to the primary and secondary gravity waves generated by a deep convective plume, *J. Geophys. Res. Space Physics*, *118*, 2377–2397, doi:10.1002/jgra.50163.

Walterscheid, R. L., and M. P. Hickey (2005), Acoustic waves generated by gusty flow over hilly terrain, *J. Geophys. Res.*, *110*, A10307, doi:10.1029/2005JA011166.

Walterscheid, R. L., G. Schubert, and D. G. Brinkman (2003), Acoustic waves in the upper mesosphere and lower thermosphere generated by deep tropical convection, *J. Geophys. Res.*, *108*(A11), 1392, doi:10.1029/2003JA010065.

Yeh, K. C., and C. H. Liu (1974), Acoustic-gravity waves in the upper atmosphere, *Rev. Geophys.*, *12*(2), 193–216.

Zettergren, M., K. Lynch, D. Hampton, M. Nicolls, B. Wright, M. Conde, J. Moen, M. Lessard, R. Miceli, and S. Powell (2014), Auroral ionospheric F region density cavity formation and evolution: MICA campaign results, *J. Geophys. Res. Space Physics*, *119*, 3162–3178, doi:10.1002/2013JA019583.

Zettergren, M. D., and J. Semeter (2012), Ionospheric plasma transport and loss in auroral downward current regions, *J. Geophys. Res.*, *117*, A06306, doi:10.1029/2012JA017637.

Zettergren, M. D., and J. B. Snively (2013), Ionospheric signatures of acoustic waves generated by transient tropospheric forcing, *Geophys. Res. Lett.*, *40*(20), 5345–5349, doi:10.1002/2013GL058018.